JGR Solid Earth

RESEARCH ARTICLE
10.1029/2023JB027590

Full-Field Numerical Simulation of Halite Dynamic Recrystallization From Subgrain Rotation to Grain Boundary Migration

B. Hao[1], M.-G. Llorens[2], A. Griera[3], P. D. Bons[4], R. A. Lebensohn[5], Y. Yu[2], and E. Gomez-Rivas[1]

[1]Departament de Mineralogia, Petrologia i Geologia Aplicada, Universitat de Barcelona, Barcelona, Spain, [2]Geosciences Barcelona, CSIC, Barcelona, Spain, [3]Departament de Geologia, Universitat Autònoma de Barcelona, Barcelona, Spain, [4]Department of Geosciences, Eberhard Karls University of Tübingen, Tübingen, Germany, [5]Materials Science and Technology Division, Los Alamos National Laboratory, Los Alamos, NM, USA

Key Points:

- The temperature-dependent transition from subgrain rotation to grain boundary migration (GBM) is simulated, reproducing torsion experiments
- Isotropic GBM changes grain size and shape but only slightly affects crystallographic preferred orientation
- The relationship between subgrain misorientation and strain is influenced by dynamic recrystallization and thus by temperature

Supporting Information:

Supporting Information may be found in the online version of this article.

Correspondence to:

E. Gomez-Rivas,
e.gomez-rivas@ub.edu

Citation:

Hao, B., Llorens, M.-G., Griera, A., Bons, P. D., Lebensohn, R. A., Yu, Y., & Gomez-Rivas, E. (2023). Full-field numerical simulation of halite dynamic recrystallization from subgrain rotation to grain boundary migration. *Journal of Geophysical Research: Solid Earth*, *128*, e2023JB027590. https://doi.org/10.1029/2023JB027590

Received 3 AUG 2023
Accepted 20 NOV 2023

Author Contributions:

Conceptualization: B. Hao, M.-G. Llorens, A. Griera, E. Gomez-Rivas
Data curation: B. Hao, M.-G. Llorens, A. Griera, E. Gomez-Rivas
Formal analysis: B. Hao, M.-G. Llorens, A. Griera, P. D. Bons, E. Gomez-Rivas
Funding acquisition: M.-G. Llorens, A. Griera, E. Gomez-Rivas
Investigation: B. Hao, M.-G. Llorens, A. Griera, E. Gomez-Rivas

Abstract Full-field numerical modeling is a useful method to gain understanding of rock salt deformation at multiple scales, but it is quite challenging due to the anisotropic and complex plastic behavior of halite, together with dynamic recrystallization processes. This contribution presents novel results of full-field numerical simulations of coupled dislocation glide and dynamic recrystallization of halite polycrystalline aggregates during simple shear deformation, including both subgrain rotation and grain boundary migration (GBM) recrystallization. The results demonstrate that the numerical approach successfully replicates the evolution of pure halite microstructures from laboratory torsion deformation experiments at 100–300°C. Temperature determines the competition between (a) grain size reduction controlled by dislocation glide and subgrain rotation recrystallization (at low temperature) and (b) grain growth associated with GBM (at higher temperature), while the resulting crystallographic preferred orientations are similar for all cases. The relationship between subgrain misorientation and strain follows a power law relationship with a universal exponent of 2/3 at low strain. However, dynamic recrystallization causes a progressive deviation from this relationship when strain increases, as revealed by the skewness of the subgrain misorientation distribution. A systematic investigation of the subgrain misorientation evolution shows that strain or temperature prediction from microstructures requires careful calibration.

Plain Language Summary Rock salt, which is dominantly composed of halite, has unique physical properties and plays a key role controlling the evolution of sedimentary basins and mountain chains. Such rocks are also important in petroleum systems, and are used for the geological storage of Geo-Energy products. However, understanding rock salt behavior is challenging because multiple deformation and recrystallization processes often operate simultaneously when halite is subjected to stress. This contribution presents microdynamic numerical simulations that replicate the main processes that take place during halite deformation at different temperatures. These include glide of dislocations, which are crystallographic defects, and temperature-controlled recrystallization processes including rotation of subgrains, nucleation of new grains, and migration of existing grain boundaries. The simulations are compared with laboratory experiments, and successfully reproduce them. Subgrain rotation is active at low temperatures, leading to the splitting of grains into smaller ones. As temperature increases, grain boundaries become mobile and grains grow to reduce the energy produced by dislocation glide. Although these processes strongly influence the resulting microstructure, the crystallographic axes are oriented similarly in all cases. We discuss how the effects of multiple microdynamic processes can be evaluated together to accurately estimate strain and the deformation conditions of rock salt.

1. Introduction

Evaporites, including rock salt, are common components of sedimentary successions and have unique physical properties such as low permeability, low density, low strength, and high ductility. Owing to these properties, salt deposits play a key role in the dynamic evolution of sedimentary basins and orogens (e.g., Canérot et al., 2005; Fossen, 2010). Their ability to flow in a viscous manner in the solid state results in the formation of structures such as salt diapirs, which cause faulting and folding of their surrounding rocks and thus often control traps in oil

Methodology: B. Hao, M.-G. Llorens, A. Griera, P. D. Bons, R. A. Lebensohn, Y. Yu, E. Gomez-Rivas
Project Administration: M.-G. Llorens, A. Griera, E. Gomez-Rivas
Resources: M.-G. Llorens, A. Griera, E. Gomez-Rivas
Software: B. Hao, M.-G. Llorens, A. Griera, P. D. Bons, R. A. Lebensohn, E. Gomez-Rivas
Supervision: M.-G. Llorens, A. Griera, E. Gomez-Rivas
Validation: B. Hao, M.-G. Llorens, A. Griera, P. D. Bons, Y. Yu, E. Gomez-Rivas
Visualization: B. Hao, M.-G. Llorens, A. Griera, P. D. Bons, E. Gomez-Rivas
Writing – original draft: B. Hao
Writing – review & editing: M.-G. Llorens, A. Griera, P. D. Bons, R. A. Lebensohn, Y. Yu, E. Gomez-Rivas

and natural gas reservoirs (Hudec & Jackson, 2007). Moreover, rock salt typically acts as detachment levels for thrusts, and determines the lateral displacement of overlying rock units and, accordingly, the dynamic evolution of orogens (McClay et al., 2004). Moreover, the dominant salt mineral halite has been extensively used as an analogue material in deformation experiments for silicate rocks and metals. This is due to its mechanical properties, which facilitate the study of deformation mechanisms at laboratory spatial and temporal scales. Specifically, halite exhibits deformation behavior that is akin to that of crustal rocks, but at substantially lower confining pressures and temperatures (Drury & Urai, 1990). Halite is also a key mineral for the energy transition, since subsurface salt bodies are targets for the storage of geo-energy products, such as hydrogen or compressed air in salt caverns. Therefore, improving our understanding of how halite deforms and recrystallizes under different conditions is essential both in terms of fundamental science, and also to meet societal challenges.

The microdynamic evolution of rock salt is controlled by the interaction between different deformation mechanisms that mostly depend on the temperature, stress/strain rate, confining pressure and water content, among others (Bourcier et al., 2013; Carter & Heard, 1970; Franssen, 1994; Franssen & Spiers, 1990; Hunsche & Hampel, 1999; Linckens et al., 2016; ter Heege et al., 2005a, 2005b; Wenk et al., 2009). At low temperature and high deviatoric stress, (semi-) brittle failure occurs in rock salt, mainly resulting in microcrack formation and propagation, and intergranular sliding (Peach & Spiers, 1996; Peach et al., 2001). As confining pressure and temperature increase cracking is suppressed, and halite deformation is dominated by dislocation creep (e.g., Urai et al., 2008). When brine is present, dislocation creep can be accompanied by dissolution-precipitation creep (Spiers et al., 1988, 1990). Dynamic recrystallization (DRX) processes accompany dislocation creep and affect the rock salt microstructure by causing changes in grain size, grain boundary network, and influencing shape-preferred orientations (SPO) (Desbois et al., 2010; Franssen, 1994; Guillope & Poirier, 1979; Mansouri et al., 2019; Schléder & Urai, 2007; ter Heege et al., 2004). DRX can result in grain size reduction or grain growth depending on the balance of driving forces involved. Grain size reduction takes place by subgrain rotation recrystallization (SGR), where the movement and reorganization of dislocations leads to the gradual increase of the local misorientation between the crystal lattices forming subgrain boundaries (low-angle grain boundaries, LAGBs), which may finally evolve to form high-angle grain boundaries (HAGBs) and the formation of new grains (Urai et al., 1986). Grain size increase is the result of grain boundary migration (GBM), a recrystallization process characterized by the migration of grain boundaries by diffusion of atoms across the boundary between grains. There are several driving forces for GBM in rocks (e.g., Bons et al., 2008). When GBM is driven by the reduction of the difference in stored strain energy (i.e., associated with dislocation densities) across the boundaries is called strain-induced GBM. During strain-induced GBM, grain boundaries migrate from grains with low dislocation density to neighboring grains with high dislocation density due to the difference in strain energy. When GBM is driven by the reduction of grain-boundary surface energy it is called surface energy-induced or boundary-energy induced GBM (Karato, 2008; Weaire & Rivier, 1984). During boundary energy-induced GBM, grain boundaries from large grains tend to overgrow small grains driven by the reduction of grain curvature, which results in grain growth (Karato, 2008). The final microstructure and grain size will depend on the competition of the interacting processes between grain size growth and reduction (Franssen, 1994; Gomez-Rivas et al., 2020; Leitner et al., 2011 and references therein).

The amount of plastic strain correlates with the probability density of subgrain misorientation angles in polycrystalline aggregates in which dislocation creep is the dominant deformation mechanism (Hughes et al., 1998, 2003, 1997; Hughes & Hansen, 2018; Pennock & Drury, 2005; Pennock et al., 2002). A scaling behavior between the mean subgrain misorientation and finite strain was proposed based on metal deformation experiments (Hughes et al., 1997), and its physical origin was established by Pantleon (1997, 1998, 2001). Pennock et al. (2005, 2002) observed that this also applies to halite and found a power-law relationship between the mean subgrain misorientation and natural strain for relatively low finite strain (up $\varepsilon = 0.54$). Their results are in agreement with numerical simulations of Mika and Dawson (1999) and Gomez-Rivas et al. (2017). This strain gauge can be a useful tool for structural analysis if it can be further tested and generalized for materials deformed under a variety of dynamic recrystallization processes, and thus at different temperatures. However, the effect of GBM on the probability density of subgrain misorientation angles has not yet been evaluated, although this recrystallization process dominates the mechanical behavior of wet rock salt in a wide range of conditions, and also of dry rock salt at relatively high temperature (Leitner et al., 2011; Trimby et al., 2000). GBM produces a reduction of intragranular heterogeneities and a significant change in the microstructure of polycrystalline aggregates (Urai et al., 1986), in a way that subgrain misorientation and the grain boundary network may not clearly reflect the strain a volume of rock has experienced (Llorens, Griera, Bons, Lebensohn, et al., 2016).

New insights into halite deformation mechanisms and rheology can be gained from laboratory experiments of natural or synthetic rock salt, and from the careful observation of samples deformed in natural settings. However, natural samples only show a "frozen" stage of the deformation history, while rock deformation experiments are inherently limited by the grain size and strain rate that can be achieved in the laboratory (e.g., Franssen, 1994; Picard et al., 2018; ter Heege et al., 2005b). Numerical simulations can overcome these barriers and are considered a key complement to these techniques. Compared to experiments, simulations allow polycrystalline aggregates to achieve significantly higher finite strains at lower strain rates, and can be used to explore a wide range of deformation conditions by varying parameters such as the sample size, strain rate, and temperature. Moreover, numerical simulations allow studying the influence of deformation mechanisms in isolation and also how they interact when they are coupled (Amelirad & Assempour, 2022; Bons et al., 2008; Eisenlohr et al., 2013; Lebensohn, 2001; Otsuka et al., 2018; Pokharel et al., 2014). Several numerical approaches have been developed to simulate dynamic recrystallization of polycrystalline materials. For example, Signorelli and Tommasi (2015) combined the viscoplastic self-consistent approach (VPSC, Lebensohn & Tomé, 1993; Liu et al., 2005; Wenk et al., 1991) with a subgrain formation probability model so as to account for SGR effects in the evolution of crystallographic preferred orientations (CPOs). In this approach, each grain is regarded as an inhomogeneity in a viscoplastic homogeneous effective medium, and therefore it does not take into account the intragranular heterogeneities for the simulation of DRX processes. Radhakrishnan and Sarma (2008) simulated DRX and the resulting CPOs in metals by coupling finite element (FEM) and Monte-Carlo (MC) approaches. However, FEM requires a high-resolution mesh to reproduce the details of heterogeneous deformation of the microstructure, which limits the use of models at larger scales due to the limitations of computational time (Roters et al., 2010). Additionally, since the changes of the microstructure in MC models occur randomly, the final texture components are highly dependent on the nucleation criterion. Another approach is the D-Rex method, which employs a kinematic constraint model to simulate dynamic recrystallization by introducing two dimensionless parameters of nucleation and GBM, but without considering mechanical interactions between grains (D-Rex, Kaminski & Ribe, 2001; Kaminski et al., 2004). All the methods mentioned above have limitations for the simulation of the evolution of the rock texture, grain boundary network and grain size.

The full-field formulation based on Fast Fourier Transforms (FFT, Moulinec & Suquet, 1994) allows overcoming the aforementioned limitations. It was initially designed to predict the mechanical properties of composite materials (Moulinec & Suquet, 1998), and was later applied to polycrystalline single-phase aggregates by Lebensohn (2001), which provided an efficient solution to model the spatial evolution of viscoplastic deformation. The Viscoplastic Full-Field Transform code (VPFFT, Lebensohn et al., 2003; Lebensohn & Rollett, 2020) and the numerical software platform ELLE (Bons et al., 2008; Jessell et al., 2001; Piazolo et al., 2019; Ran et al., 2018) were integrated for the large-strain full-field simulation of dislocation creep (Griera et al., 2011, 2013). The numerical scheme comprises a variety of dynamic recrystallization processes, including intracrystalline recovery, grain nucleation, and GBM, by mapping misorientations between local lattice orientations on a regular grid. This full-field numerical modeling approach has been widely used to model the evolution of microstructure of polycrystals such as 1-h ice and halite, as well as multiphase anisotropic rocks (Finch et al., 2022; Gomez-Rivas et al., 2017; Llorens, Griera, Bons, Lebensohn, et al., 2016; Ran et al., 2022; Steinbach et al., 2016).

This contribution presents VPFFT-ELLE simulations of the deformation of halite polycrystalline aggregates at 100°C, 200°C, and 300°C including SGR and GBM recrystallization processes, up to a finite shear strain (γ) of four. The simulations are calibrated by comparing them with torsion experiments of synthetic pure rock salt by Armann (2008). Moreover, we investigate how the interplay between SGR and GBM processes influences grain size and grain morphology at different temperatures. In addition, we estimate the subgrain misorientation of whole grains and evaluate the use of the geometric mean of subgrain misorientation as a strain gauge for systems deformed at different temperatures and, therefore, under different recrystallization processes (i.e., SGR vs. GBM-dominated). This approach allows to systematically visualize and quantify the influence of temperature on rock deformation, test how different recrystallization processes affect strain gauges, and analyze whether subgrain misorientations can be utilized to reveal the environmental conditions under which rocks deform.

2. Methods

2.1. ELLE Numerical Platform

ELLE is an open-source multi-scale software used to simulate the evolution of microstructures during deformation and metamorphic processes (http://www.elle.ws). So far, it has been widely used to simulate a variety

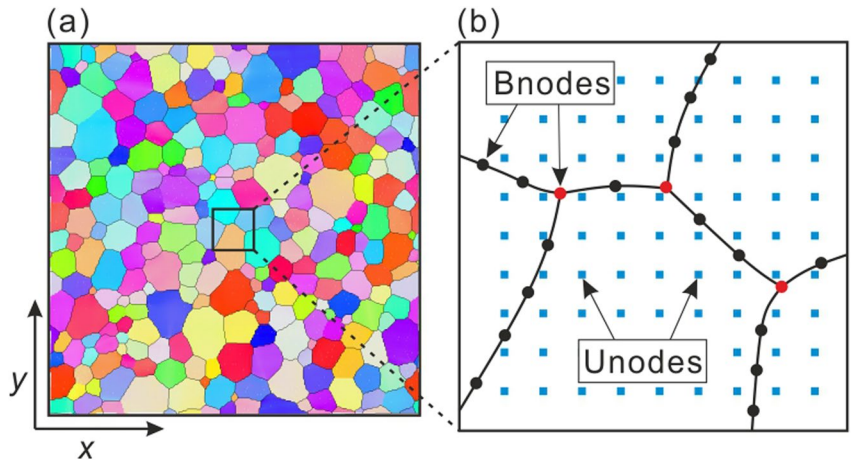

Figure 1. (a) Initial microstructure used in this study, and (b) maximization showing the discretization in two layers of unconnected nodes (*unodes*) and boundary nodes (*bnodes*) used in the numerical approach. Each color in (a) represents a different crystallographic orientation.

of microstructural processes, such as static grain growth (Jessell et al., 2003; Roessiger et al., 2011), dynamic recrystallization (Gomez-Rivas et al., 2017; Llorens, Griera, Bons, Roessiger, et al., 2016, 2017; Steinbach et al., 2016, 2017), strain localization (de Riese et al., 2019; Griera et al., 2011), rotation of rigid objects in anisotropic rocks (Griera et al., 2013; Ran et al., 2019), or deformation of multiple phase materials (Finch et al., 2020, 2022; Jessell et al., 2009; Llorens et al., 2019; Ran et al., 2018; Steinbach et al., 2017) among many other studies. A comprehensive introduction to the ELLE principles and modeling approach can be found in Bons et al. (2008) and more recent developments in the review by Piazolo et al. (2019).

Here the data structure of ELLE is only briefly introduced, and the reader is referred to the aforementioned reviews for more details. In ELLE, a 2D polycrystalline aggregate (Figure 1a) is discretized in two data layers as shown in Figure 1b: (a) a periodic grid formed by unconnected nodes (*unodes*) or Fourier points, which are regarded as crystallites (i.e., the smallest unit with homogeneous properties) and used to store physical properties such as dislocation density, local stress, or local lattice orientation, among other parameters, and (b) a set of continuous polygons that are here defined as grains, defined by boundary nodes (*bnodes*) and straight line segments linking them. These boundary nodes can move to simulate GBM.

ELLE uses an operator-splitting approach (Becker et al., 2008; Bons et al., 2008), whereby the initial data file goes through a loop of sequential processes at each time step of the simulation (Figure 2). This loop includes deformation by dislocation glide, using the VPFFT approach, and all DRX processes organized in a subloop. On top of these main processes, other routines are used for data management, data conversion, and topology checks. The next section provides an overview of the processes used in this study. ELLE and VPFFT use periodic boundaries, where the left and right parts of the model unit cell, as well as the upper and lower ones, are connected and continuous (Jessell et al., 2001). After each deformation step, the areas that fall out of the square unit cell are repositioned back into the unit cell (Reposition, Figure 2). This approach allows visualizing the microstructure even at very high shear strains.

2.2. VPFFT—Viscoplastic Deformation by Dislocation Glide

The VPFFT (Lebensohn, 2001) is a suitable and widely used method for solving problems in the field of micromechanics. The approach is based on the application of Green functions to transform and solve the mechanical problem by means of the fast Fourier transform algorithm. The approach minimizes the average local work rate under the constraints of compatibility and equilibrium by finding an admissible stress and strain rate field. A detailed explanation of the VPFFT method can be found in Lebensohn (2001) and Lebensohn and Rollett (2020), and its implementation in ELLE is described by Griera et al. (2013). The VPFFT is a spectral method that discretizes the polycrystalline aggregate into a periodic rectangular grid composed of Fourier points. This approach assumes that the crystalline deformation of the polycrystalline aggregate is only achieved by dislocation slip

Table 1
Input Properties of Numerical Simulations

Symbol	Explanation	Input value
	Unit length	3×10^{-3} m
	Minimum *bnode* separation	3.96×10^{-5} m
	Maximum *bnode* separation	1.8×10^{-5} m
	Time step per simulation step	100 s
	Incremental strain per simulation step	0.03
n	Stress exponent (Carter & Heard, 1970)	7
$\tau_{\{110\}}$	Critical resolved shear stress of $\{110\} < \bar{1}10 >$ slip system (Carter & Heard, 1970)	1
$\tau_{\{111\}}$	Critical resolved shear stress of $\{111\} < \bar{1}10 >$ slip system (Carter & Heard, 1970)	2
$\tau_{\{100\}}$	Critical resolved shear stress of $\{100\} < 011 >$ slip system (Carter & Heard, 1970)	3
b	Burgers vector (Frost & Ashby, 1982)	3.9×10^{-10} m
G	Shear modulus	7.1×10^{9} Pa
M_0	Intrinsic mobility (Piazolo et al., 2006; Sun & Bauer, 1970)	1.5×10^{-7} m^4 J^{-1} s^{-1}
Q	Grain boundary migration activation energy (Piazolo et al., 2006)	4.7×10^{4} J mol^{-1}
J	Boundary energy (Bruno et al., 2008) (average value)	0.36 J m^{-2}
α_{hagb}	Critical minimum misorientation for halite high-angle boundaries (Pennock et al., 2005)	10°

along predefined slip systems of the crystal. The calculation of stress $\sigma'(\mathbf{x})$ and strain rate $\dot{\varepsilon}_{ij}(\mathbf{x})$ at each Fourier point obeys a nonlinear viscous rate-dependent power law based on the strength of the different slip systems. The constitutive equation is given by:

$$\dot{\varepsilon}_{ij}(\mathbf{x}) = \sum_{s=1}^{N_s} m_{ij}^{s}(\mathbf{x})\dot{\gamma}^{s}(\mathbf{x}) = \dot{\gamma}_0 \sum_{s=1}^{N_s} m_{ij}^{s}(\mathbf{x}) \left| \frac{m^{s}(\mathbf{x}) : \sigma'(\mathbf{x})}{\tau^{s}(\mathbf{x})} \right|^{n} \mathrm{sgn}\left(m^{s}(\mathbf{x}) : \sigma'(\mathbf{x})\right), \quad (1)$$

where N_s is the number of all slip systems in the crystal, m_{ij}^{s} is the symmetric Schmid tensor, $\dot{\gamma}^{s}$ is the shear strain rate, $\dot{\gamma}_0$ is a reference strain rate, τ^{s} is critical resolved shear stress for the slip system s, and n is the stress exponent. Here we use an exponent of $n = 7$ for all the slip systems (Table 1). The actual stress exponent (n) obtained from torsion experiments ranges from 4.5 to 5.4 (Armann, 2008), which is consistent with the n values (4.1–13.2) obtained from other experiments (Carter et al., 1993; Franssen, 1994; Marques et al., 2013; Wawersik & Zeuch, 1986). In order to be consistent with previous halite viscoplastic simulations (e.g., Gomez-Rivas et al., 2017) all simulations presented here are carried out with $n = 7$.

2.3. ELLE—Recrystallization Processes

The simulation of recrystallization processes is applied in a subloop with three main numerical modules that simulate polygonization, GBM, and intracrystalline recovery. The polygonization module determines whether to generate new HAGBs if the misorientation angle of a cluster of *unodes* (i.e., subgrain) is higher than a predefined threshold. The movement of HAGBs is applied by the GBM code (Becker et al., 2008; Llorens, Griera, Bons, Roessiger, et al., 2016), which calculates their displacement based on the grain boundary energy and the intragranular strain stored energy as driving forces. The intracrystalline recovery process is driven by the reduction of the local misorientation and associated energy of dislocation densities, and reproduces the annihilation of dislocations and their rearrangement into LAGBs (Borthwick et al., 2014; Gomez-Rivas et al., 2017). It is worth noting that the *unodes* in ELLE code and the Fourier points in VPFFT have a one-to-one mapping relationship, where the physical properties stored in *unodes* and Fourier points can be directly transferred between the ELLE and VPFFT code (Griera et al., 2013).

2.3.1. Polygonization

In the polygonization process, new grains are defined as clusters of *unodes*, in a way that the misorientation between them and that of adjacent clusters is greater than the predefined misorientation threshold (HAGB),

which is set to 10° following Pennock et al. (2005). The polygonization routine detects clusters with misorientation higher than the predefined threshold and inserts new boundary nodes between them to segment the preexisting grain. Specifically, the approach uses Voronoi tessellations of the *unode* layer clipped to the preexistent grain boundaries to define new positions of *bnodes* from a cluster of critical *unodes*. The new grain is therefore defined as a small part of a preexistent grain and, therefore, preserves the topology of the grain network. Two main restrictions are imposed in this approach: (a) island grains (i.e., new grains within old grains) are not allowed to prevent topology misfits and (b) a minimum of four *unodes* are required to create a new grain in order to prevent numerical instabilities due to lack of information inside the new grain. The reader is referred to Steinbach et al. (2016) for a more detailed description of this numerical process.

2.3.2. Grain Boundary Migration (GBM)

The GBM code used in this contribution is the same as the one described in Llorens, Griera, Bons, Lebensohn, et al. (2016) and Steinbach et al. (2016). This subsection provides an overview of the process, but a more detailed explanation of the approach and its implementation can be found in Becker et al. (2008) and Llorens, Griera, Bons, Roessiger, et al. (2016). The driving forces used to move HAGBs are the reduction of grain boundary energy and intragranular strain energy. The driving stress (ΔF) can be expressed as:

$$\Delta F = \Delta H - \frac{2J}{r}, \tag{2}$$

where J is the boundary energy and r is the local radius of curvature of the grain boundary. ΔH is the differential strain stored energy across a grain boundary, which is calculated from the shear modulus (G, assumed to be isotropic), the Burgers vector (b), and the difference in dislocation density ($\Delta\rho$):

$$\Delta H = \Delta\rho G|b|^2. \tag{3}$$

The velocity of a grain boundary (v) is calculated from the grain boundary mobility (M) and driving stress (ΔF):

$$v = M\Delta F\vec{n}, \tag{4}$$

where $\vec{n}$ is the unit vector perpendicular to the boundary. M has an exponential relationship with temperature (T), which is calculated from the GBM activation energy (Q), the intrinsic mobility (M_0), and the universal gas constant (R):

$$M = M_0 \exp^{(-Q/RT)}. \tag{5}$$

The GBM code is based on the front-tracking method of Becker et al. (2008), which moves the boundary nodes (*bnodes*) to achieve a reduction of Gibb's free energy. This direction is determined using four orthogonal trial positions close to the current *bnode* position and determining the gradient of energy reduction in x and y directions. In the area swept by the grain boundary movement, the dislocation density ρ is set to 0. All parameters involved in GBM are listed in Table 1.

2.3.3. Intracrystalline Recovery

This module simulates intracrystalline recovery, reproducing the annihilation of dislocations and their rearrangement into LAGBs. This approach assumes that intracrystalline heterogeneities in the lattice orientation produce a local increase of the effective interface energy of low angle boundaries. The reduction of local misorientation produces a reduction of the free energy of the system. The approach assumes that the rotation rate of the *unode* or crystallite is proportional to the torque (Randle, 1993), and follows a linear viscous rate law (i.e., linear relationship between shear stress and strain rate) (Gomez-Rivas et al., 2017). For a random *unode* chosen, the module only considers the first-neighbor *unodes* belonging in the same grain (i.e., *unodes* with a local misorientation angle lower than HAGB). The routine calculates for each *unode* the local misorientation and boundary energy with respect to the neighbor *unodes* following the Read-Schockley equation (Read & Shockley, 1950). Then, a small increment of the lattice orientation (in our simulations 0.02°) of the reference *unode* is applied using sample directions as rotation axis. The reference *unode* crystal orientation is changed toward the value that accounts for the maximum energy reduction. For a detailed description of the recovery module, the reader is referred to Borthwick et al. (2014) and Gomez-Rivas et al. (2017) (including the supplementary material of the latter publication).

Table 2
Numerical Simulation Setup

Simulation name	Temperature (°C)	Recovery/polygonization/ GBM/VPFFT steps*	Initial average grain size (μm)	Final average grain size (μm)	Equivalent final time (s)/Shear strain	Strain rate (s^{-1})
G10_100	100	0/0/10/0	212	212	13,300/0	0
G10_200	200	0/0/10/0	212	223	13,300/0	0
G10_300	300	0/0/10/0	212	299	13,300/0	0
DRX_100	100	5/20/10/1	212	92	13,300/4	3×10^{-4}
DRX_200	200	5/20/10/1	212	135	13,300/4	3×10^{-4}
DRX_300	300	5/20/10/1	212	303	13,300/4	3×10^{-4}

Note. * indicates the number of subloops of the different processes during one simulation step. The suffix of the simulation name indicates the temperature.

2.4. Validation of the Numerical Setup With Experimental Results

In order to calibrate our modeling approach, torsion experiments of synthetic rock salt by Armann (2008) have been compared with the results of our simulations. The parameters analyzed include, but are not limited to, grain size statistics, crystallographic orientation maps, and pole figures. The halite polycrystalline aggregate used in the experiments of Armann (2008) (with a water content of 35 ppm, determined by Fourier transform infrared spectroscopy—FTIR) consisted of isotropic polygonal crystals with an initial average grain size of 216 μm. Cylindrical samples with a diameter of 15 mm were cored from the starting material and dried at atmospheric pressure and 110°C for at least 24 hr before testing (following the protocol by Marques et al., 2013). The torsion experiments were conducted in a temperature-controlled triaxial deformation Paterson rig (Paterson & Olgaard, 2000). Shear strain rate and shear strain increase linearly in the torsion experiments from the sample's central axis to the outer circumference, and any position of the sample can be regarded as undergoing approximate simple shear deformation. The experiments of Armann (2008) were carried out at three sets of constant twist rates, corresponding to nominal strain rates of 3×10^{-3}, 3×10^{-4}, and 3×10^{-5} s^{-1}, respectively. The samples were deformed up to a shear strain of eight at 100°C, 200°C, and 300°C, with a constant confining pressure of 250 MPa. The reader is referred to Armann (2008) and Marques et al. (2013) for a more detailed description of their experimental setup.

The setup of our simulations is similar to those of these laboratory experiments, including the initial grain size, boundary conditions, temperature ranges, and strain rates, in order to allow a direct comparison. Specifically, a 3×3 cm^2 initial foam structure consisting of 255 grains was discretized into a grid of 256×256 *unodes* (Fourier points or crystallites), resulting in a unit cell defined by 65,536 *unodes* (Figures 1a and 1b). The initial average grain diameter of our model is 212 μm (Table 2). The starting material is considered isotropic, as the initial distribution of lattice grain orientations is random (Figure 1a). A detailed summary of all the input parameters for the simulations is presented in Table 1. For parameters not listed there, the input parameters used by Llorens, Griera, Bons, Roessiger, et al. (2016) were adopted (see their Table 1).

In this study we simulated the microstructure evolution of pure halite at different temperatures (100°C, 200°C, and 300°C) under dextral simple-shear deformation up to a finite shear strain of $\gamma = 4$, by the application of shear strain increments of $\Delta\gamma = 0.03$ in each time step, followed by a subloop of recrystallization processes (Figure 2) where different recrystallization modules were called (Table 2). Initially, a set of simulations that activate the DRX subloop with 5 times recovery, 20 polygonization, and 10 times GBM per deformation time step (see DRX simulations in Table 2) were done for comparison with the experiments. In order to check the equivalent time and influence of GBM (details are in Section 3.1), a set of simulations without deformation and with only GBM (static grain growth) were carried out (see G10 simulations in Table 2). In these simulations only the boundary energy was used as a driving force to calculate grain boundary displacement. By activating each module in turn, the microstructure undergoes a loop of deformation processes within a constant time step ($\Delta t = 100$ s). The simulations go through a total of 133 loops up to shear strain of 4, so the equivalent total time is 13,300 s and the shear strain rate is $\dot{\gamma} = 3 \times 10^{-4}$ s^{-1} for all simulations.

Lattice orientation and other data generated after each of the simulation steps were post-processed using the texture analysis software MTEX (http://mtex.googlecode.com; Bachmann et al., 2010; Mainprice et al., 2011) to

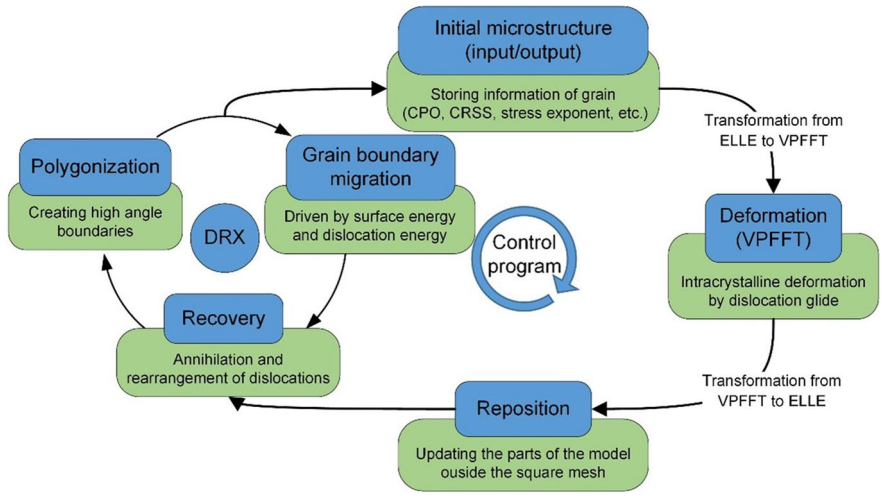

Figure 2. Loop showing the process workflow for one simulation time step. The initial microstructure is first subjected to viscoplastic deformation (VPFFT), followed by reposition, and a subloop of dynamic recrystallization processes (DRX). The DRX subloop includes polygonization, grain boundary migration (GBM), and intracrystalline recovery.

map the crystallographic textures (i.e., crystallographic preferred orientation maps, pole figures), analyze grain boundary misorientations, and the grain size network.

3. Results

3.1. Static Grain Growth

Static grain growth is simulated as GBM driven exclusively by grain boundary energy reduction (without considering GBM induced by dislocation stored strain energy; Karato, 2008; Weaire & Rivier, 1984). The kinetics of this process can be defined by the average area A from an initial area A_0 (Bons & Urai, 1992; Olgaard & Evans, 1988):

$$A - A_0 = MJt, \tag{6}$$

where M is the grain boundary mobility according to Equation 4, J is the grain boundary energy, and t is time. The total time is equivalent to the duration of the experiments of Armann (2008) (approx. 13,300 s). The input parameters are presented in Tables 1 and 2. We assume surface and grain boundary energies to be equal. This implies a strong binding energy between surfaces (e.g., Rohrer, 2011). The simulations only including static grain growth (G10_100, G10_200, and G10_300 simulations) are used to test the validity of the setup of the GBM model, by comparing it with the theoretical calculation following Equation 6. As shown in Figure 3, and taking G10_300 as an example, the average grain diameter (as a proxy of grain size) in the simulation increases from 212 to 299 μm after 13,300s, while that following the theoretical calculation raised to 303 μm for the same time (Table 2 and Figure 3, red lines). The diameter-time curves of G10_100 and G10_200 are also in agreement with the theoretical curves (Figure 3, blue and green lines). Compared with the significant grain growth of the G10_200 and G10_300 simulations, those of the G10_100 simulation do not change during the limited equivalent time. This reveals that the ratio GBM/VPFFT of 10 steps is correct, and validates the selected GBM parameters for our simulations (Table 2).

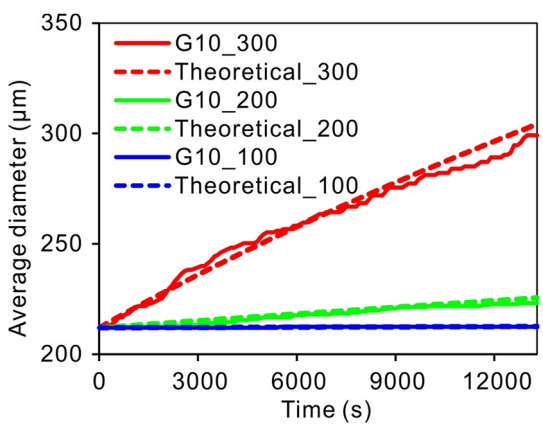

Figure 3. Evolution of the average grain size for simulations with only GBM (G10 simulations, solid lines) compared with the theoretical calculation (dashed lines) at temperatures of 100°C (blue), 200°C (green) and 300°C (red).

Analysis of the grain boundary orientation distribution of slightly deformed polycrystalline aggregates of synthetic rock salt using EBSD reveals that grain boundaries show a preference for {110} planes, which may be related to the anisotropy of the grain boundary energy (Pennock et al., 2009). Our

study assumes that all planes per unit length have the same grain boundary energy (i.e., isotropic) and, therefore, we refer to GBM driven by isotropic grain boundary energy (and dislocation energy) as isotropic GBM to distinguish it from natural and synthetic rock experiments. Figures 4l–4n show the microstructure of the simulations with static grain growth driven by grain boundary energy at equivalent time of 10,000 s (G10_100, G10_200, and G10_300 simulations). All static grain growth simulations produce classical foam texture patterns, similar to the starting mineral aggregate (Figure 3a), which is coherent with the isotropic boundary energy setup considered in this initial set of simulations.

3.2. Microstructure Evolution

Simulations DRX_100, DRX_200, and DRX_300 represent systems in which dislocation creep and dynamic recrystallization processes (i.e., intracrystalline recovery, polygonization and GBM) are coupled at various temperatures (100°C, 200°C, and 300°C). At low temperatures (100°C and 200°C) grain boundaries tend to be elongated and parallel to the stretching direction, showing a SPO oblique to the shear plane (Figures 4f, 4g and 4b). As expected, the angle between the SPO and the shear plane gradually decreases with progressive deformation, and at shear strain of three the foliation already lies at a low angle with respect to the shear plane (approximately 17°, Figures 4i, 4j and 4b). At high temperatures (300°C), elongated grains parallel to the stretching direction and SPO are still visible, but their aspect ratio is lower, and grains are larger and more equidimensional than those of the low-temperature models at a similar shear strain (100°C and 200°C) (Figures 4k and 4b). At low temperatures, the initial grain size (Figure 4a) decreases significantly with increasing strain due to polygonization of new (recrystallized) grains (Figures 4i and 4j, Table 2), and an intense network of LAGBs can be recognized within relict grains, as shown in Figures 4i and 4j. The density of the LAGB network gradually increases with progressive strain, revealing a general trend of increasing intergranular heterogeneities with deformation (Figures 4i and 4j). However, increasing GBM weakens this trend, resulting in a lower density of LAGBs (e.g., Figure 4k).

A close look at the evolution of the grain boundary network more clearly reveals the effect of temperature on DRX. A detail of the grain boundary map of a small area of the simulations is shown in Figure 5 for the 100°C (DRX_100) and 300°C (DRX_300) cases. Increasing temperature accelerates GBM and reduces the number of LAGBs. At low shear strain ($\gamma = 0.3$) the microstructures show similar grain boundary and subgrain boundary networks regardless of the temperature (Figures 5a and 5d, red circle). With progressive strain grains split into multiple new grains at 100°C, as a consequence of the increase in local misorientation of the LAGBs (Figures 5b and 5c). However, at 300°C, and for an equivalent region of grains to that of the 100°C case, there is a tendency of the grains with stronger substructure heterogeneities to disappear before they accumulate enough misorientation to split and produce new grains. The effect of GBM at high temperature is observed in Figures 5d–5f, where the boundaries of grains containing no or few low-angle grain boundaries move toward grains with higher subgrain heterogeneities, so that the substructures rich of grains are consumed and eventually disappear (Figure 5f, red arrow). A similar process is visible in the blue circles of Figure 5.

The evolution of grain size distribution during progressive deformation is shown in Figure 6, where the frequencies of grain size fractions are represented by different colors. The statistical results show that the grain size distribution in logarithmic scale is always unimodal at different temperatures. At 100°C and 200°C (Figures 6a and 6b) the grain size distribution shifts toward smaller grain sizes. Specifically, the proportion of small grains gradually increases with progressive deformation (Figure 6, log grain size ranges between 1.4 and 2.0), while the proportion of large grains gradually decreases (Figure 6, log grain size ranges between 2.0 and 2.6), revealing that the grain refinement process dominated by SGR induces grain size reduction. The situation at 300°C is different because the grain size distribution reveals larger grain sizes, and is basically stable for the logarithmic grain-size range of 2.4–2.6, remaining constant at around 30% with increasing shearing (Figure 6c). The grain size distribution of the 200°C model is more uniform than that of the 100°C case at high strain ($\gamma > 2$), possibly due to the large effective mobility of GBM at higher temperatures. The population of small grains remains essentially unchanged with increasing shear strain at 300°C (Figure 6c, log grain size ranges between 1.2 and 1.6), which is different from that of the low-temperature models (100 and 200°C), whose proportions gradually increase.

3.3. CPO Evolution

The crystallographic preferred orientation maps of DRX simulations (Table 2) at different shear strains ($\gamma = 1$, 2, 3) and different temperatures ($T = 100$°C, 200°C, 300°C) are shown in Figure 4, while the pole figures of the CPOs are plotted in Figure 7. As shown in Figures 4 and 7, the CPO evolution with progressive strain

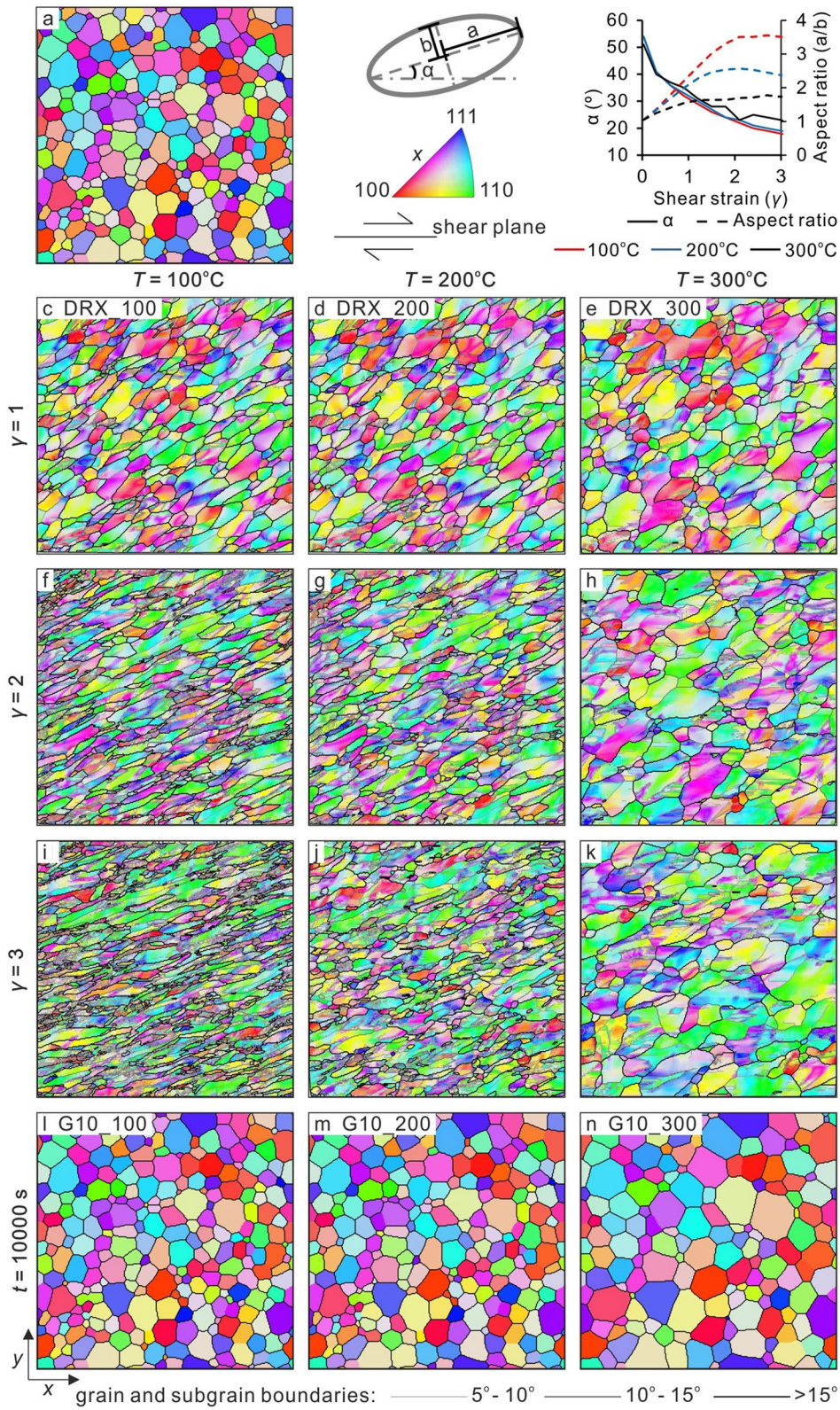

Figure 4.

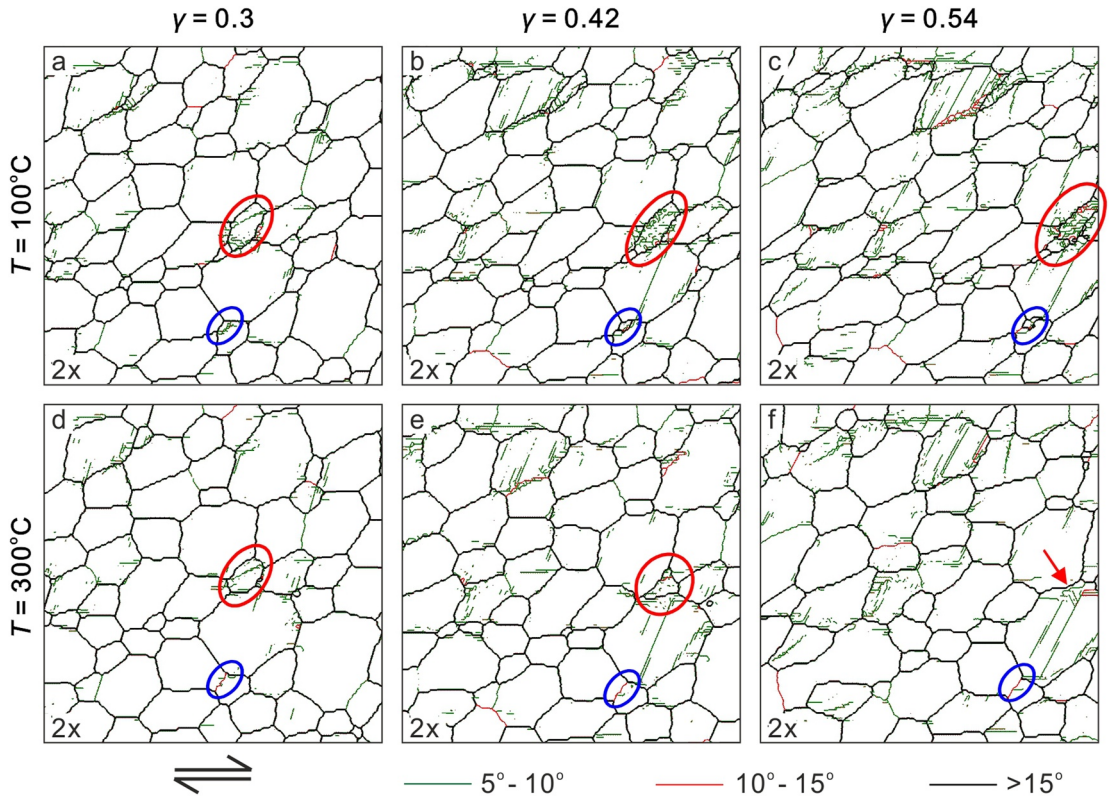

Figure 5. Comparison of the details of the grain boundary evolution of a selected grain with fully activated dynamic recrystallization processes (DRX) at shear strains of $\gamma = 0.3$, 0.42, and 0.54 at 100°C (a–c) and 300°C (d–f), respectively.

is very similar regardless of the temperature. Pole figures show the progressive evolution and intensity of the initial random distribution of crystallographic orientations (Figure 7a), which in all cases evolve to form a {100} maximum CPO approximately perpendicular to the shear plane and two maxima at approximately 45° to it (Figures 7d, 7g and 7j). At low strain ($\gamma = 1$), the {100} pole figure shows two maxima. One of these maxima is obliquely oriented to the shear plane with the opposite sense of shear, and the other one is approximately perpendicular to it ($\gamma = 1$, Figures 7b, 7e and 7h). For the same shear strain, the {110} and {111} pole figures show a weak hexagonal symmetry (Figures 7b, 7e and 7h). The {110} CPO evolves with shear strain to form two maxima parallel to the shear plane and other four maxima oriented at 45° from it (Figures 7d, 7g and 7j). The {111} CPO evolves toward a pattern with four maxima at 45° to the shear direction. The {110} and {111} CPO intensity increases when temperature raises (compare Figures 7d, 7g and 7j). However, the intensity of the final {100} CPO oriented perpendicular to the shear plane is reduced while the intensity of the two maxima oblique to the shear plane increases (Figures 7d, 7g and 7j). Dynamic recrystallization does not change the CPOs, but shows a reduction of dispersion of crystallographic axes and strengthening of the maxima (Figure 7).

4. Discussion

The objective of this study is to investigate the microstructural evolution of halite aggregates in simple shear viscoplastic deformation including DRX at different temperatures, and compare numerical predictions with torsion experiments. We calibrate and corroborate that full-field DRX simulations are able to reproduce results from the experiments of Armann (2008). Specifically, the grain size statistics (Figures 6 and 8), microstructures,

Figure 4. Crystallographic orientation and grain and subgrain boundary network maps of simulations with fully activated dynamic recrystallization processes (DRX) at different shear strains ($\gamma = 1, 2, 3$) at (c, f, i) 100°C, (d, g, j) 200°C, and (e, h, k) 300°C, and simulations with only GBM at a time $t = 10{,}000$s and at (l) 100°C, (m) 200°C, and (n) 300°C, respectively. The initial microstructure is shown in (a). Crystal lattice orientations are plotted as inverse pole figure colors with respect to the horizontal x axis (the shear direction). (b) Evolution of average shape-preferred orientation (solid lines indicate the angle between the major axis and the shear direction, while dashed lines the aspect ratio) with shear strain from $\gamma = 0.03$ to $\gamma = 3$ at 100°C (red lines), 200°C (blue lines), and 300°C (black lines).

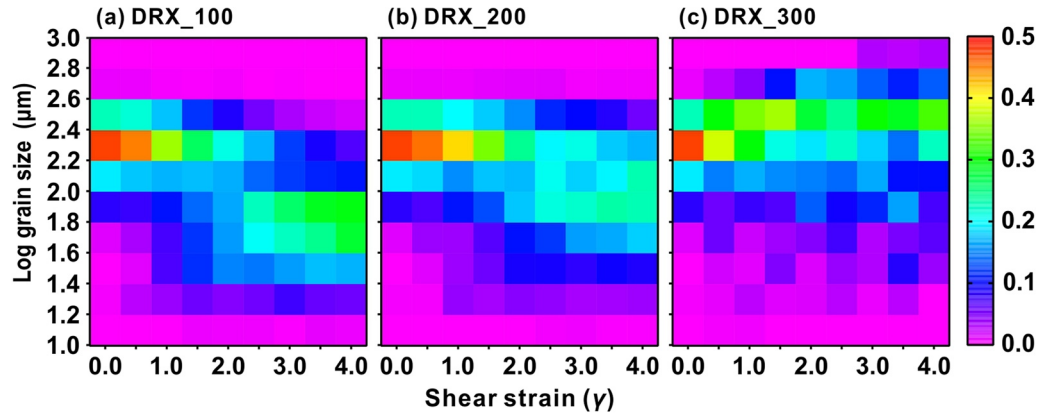

Figure 6. Evolution of grain size distribution with progressive strain for the simulations with fully activated dynamic recrystallization processes (DRX) (DRX_100/200/300). The grain size corresponds to the equivalent grain size (in logarithmic form, $\log_{10}$).

and crystallographic orientation maps (Figures 4 and 7) of our numerical models can be directly compared with those from the pure halite torsion experiments of Armann (2008) and Marques et al. (2013) at the same temperature range (Figure S1 in Supporting Information S1). The simulations presented here also match the numerical results from VPSC simulations of Wenk et al. (2009) and full-field simulations of Gomez-Rivas et al. (2017), expanding the range of simulation conditions to include GBM recrystallization during halite deformation.

4.1. Effect of Temperature on the Evolution of Microstructures

Under static conditions, when grain growth is purely driven by isotropic grain boundary energy reduction (Equation 6) (G10 simulations), the resulting microstructure is a typical foam texture (e.g., Weaire & Rivier, 1984) similar to those reported for undeformed rock salt after heating experiments by Bestmann et al. (2005). Under dynamic recrystallization conditions (DRX simulations), we can observe how temperature determines the balance between grain size reduction/growth, significantly affecting the microstructure evolution of halite polycrystalline aggregates at a constant shear strain rate. When the microstructure is deformed at high-temperature

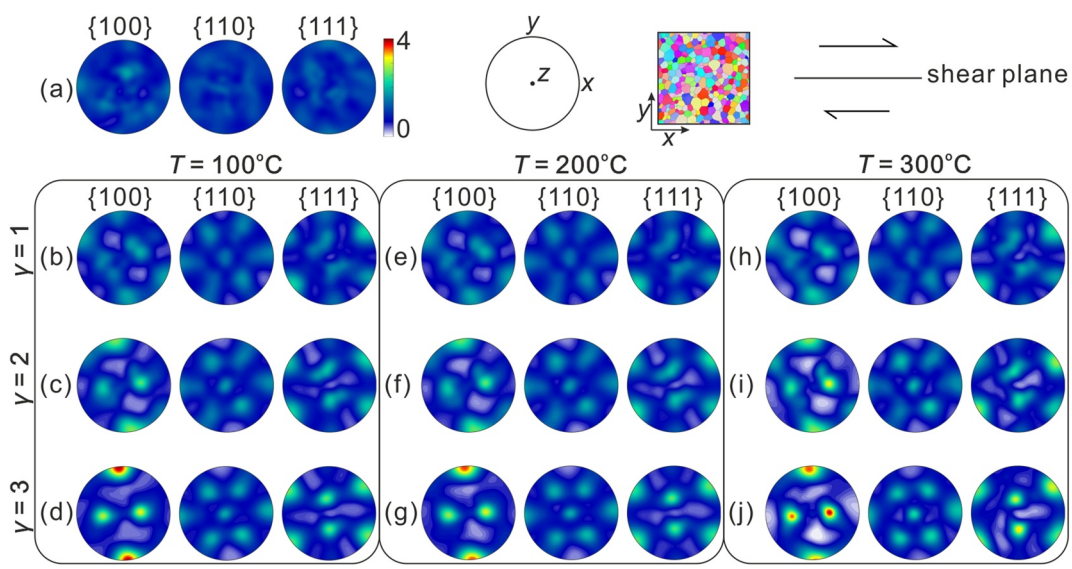

Figure 7. Pole figures of the crystallographic preferred orientations (CPOs) during deformation, where the shear sense is dextral and the shear plane is horizontal. The stereoplots of (a) correspond to the initial stage. Stereograms of the three groups of columns show the CPO evolution for the simulations with fully activated dynamic recrystallization processes (DRX) (DRX_100/200/300) at different shear strains (γ = 1, 2, 3) at (b–d) 100°C, (e–g) 200°C, and (h–j) 300°C, respectively.

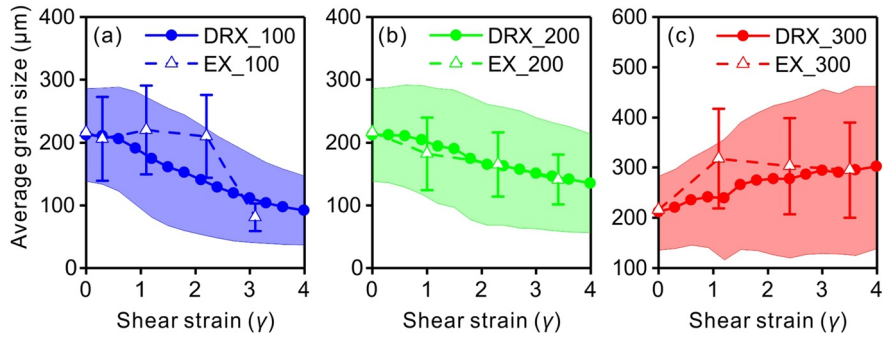

Figure 8. Comparison of evolution of the average grain size (solid lines) with its standard deviation (shaded areas) for simulations (DRX_100/200/300) run in this study at (a) 100°C, (b) 200°C, and (c) 300°C with laboratory experiments of Armann (2008) (dashed lines with error bars, EX_100/200/300) at the same temperatures. All the models and experiments were run at shear strain rate of 3×10^{-4} s^{-1}.

conditions (300°C), GBM produces a larger average grain size than that of the initial microstructure, while when the models are run at lower temperatures (100°C and 200°C) (Table 2, Figures 8a and 8b) grain size reduction is clearly observable (Armann, 2008). Moreover, there are more equidimensional grains at 200°C than at 100°C (Figure 4b), showing that temperature-dependent GBM strongly affects the grain shapes. The transition from low (100°C and 200°C) to high temperature (300°C) in our numerical microstructures is comparable with that taking place in quartz deformation experiments from the regime II to regime III of Stipp et al. (2002). Regime II is dominated by SGR, in which a portion of LAGBs eventually evolve to HAGBs, and with the formation of new grains due to the gradual increase of dislocations within grains as a result of dislocation movement and reorganization (Hirth & Tullis, 1992; Urai et al., 1986). Regime III is characterized by a significant increase in grain boundary mobility at higher temperature and large recrystallized grains (Stipp et al., 2010).

The grain size evolution of the laboratory experiments of Armann (2008) versus our simulations at 100°C, 200°C, and 300°C at a shear strain rate of 3×10^{-4} s^{-1} is shown in Figure 8 (grain size mean and standard deviation). The numerical simulation average grain size at different temperatures is basically consistent with that of the torsion experiments. It gradually decreases with increasing shear strain for the low-temperature systems (100°C and 200°C) (Figures 8a and 8b), while it increases when temperature is higher (300°C) (black line in Figure 8c). The reduction rate of the grain diameter standard deviation of simulations is significantly lower than the estimated value of the experiments (Armann, 2008). This reveals that the grain size distribution in our simulations during progressive strain is more inhomogeneous than that in experiments (Armann, 2008). One of the reasons may be that the discontinuous GBM processes affected by grain boundary pinning may limit the growth of large grains in laboratory experiments (Guillope & Poirier, 1979; Lücke & Stüwe, 1971), while impurity pinning processes are not included in our simulations. Deformation annealing experiments of rock salt (Piazolo et al., 2006) convincingly show that GBM is sensitive to changes in solute impurities or the substructure when the temperature is lower than 400°C.

Our results reveal that grains with a large number of subgrain boundaries are consumed by grains with no or few low-angle grain boundaries (Figure 5). This is a phenomenon similar to that described from halite laboratory experiments (Armann, 2008; ter Heege et al., 2005b) and borehole sample observations (Henneberg et al., 2020; Schléder & Urai, 2005; Thiemeyer et al., 2016). Our simulations assume that the rate of GBM has an exponential relationship with temperature. As expected, the GBM rate increases rapidly with increasing temperature and dominates rock salt deformation, potentially resulting in a microstructure reset (Franssen, 1994; Leitner et al., 2011).

4.2. Effect of Temperature on the Crystallographic Preferred Orientation (CPO) Evolution

The numerical CPO evolution (Figures 7b–7g) at low temperature is similar to those of the rock deformation experiments at 100°C and 200°C of Armann (2008) (Figure 9), and to numerical simulations by Wenk et al. (2009). However, the models at higher temperature (300°C) (Figure 7h) differ from the experimental results of Armann (2008) (see discussion in the next paragraph below). Strong CPOs develop rapidly with progressive

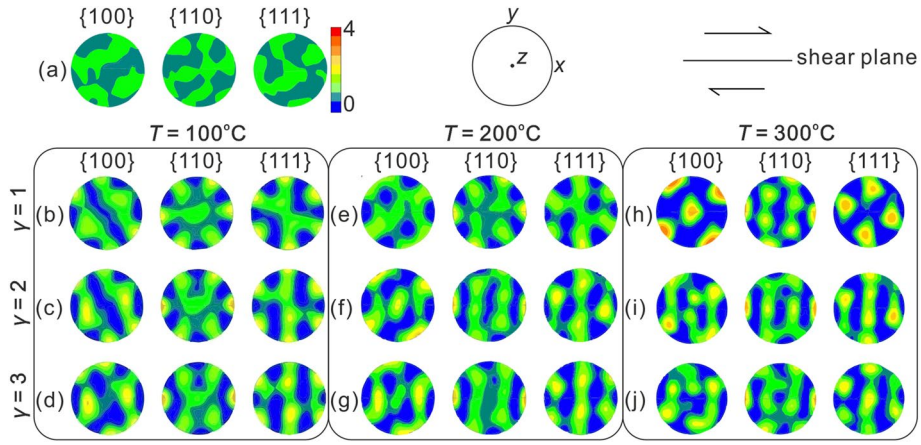

Figure 9. Pole figures of the crystallographic preferred orientations (CPOs) from torsion experiments (Armann, 2008). The stereoplots of (a) correspond to the initial stage. Stereograms of the three groups of columns show the CPO evolution for the torsion experiments at different shear strains ($\gamma = 1, 2, 3$) at (b–d) 100°C, (e–g) 200°C, and (h–j) 300°C, respectively.

deformation for the whole series of experiments, regardless of whether GBM was active or not (Figure 7). The initial randomly distributed CPOs quickly evolve into a pole to {100} sub-perpendicular to the shear plane at lower strain of 2 (Figures 7c, 7f and 7i). The {100} maximum then gets rotated according to the sense of shear up to becoming perpendicular to the shear plane at high shear strain ($\gamma = 3$) (Figures 7d, 7g and 7j). The results of our simulations show that isotropic GBM has a very limited effect on the CPOs, with the only effect that there is less scattering and more intense pole of lattice orientation in higher temperature systems (Figure 7). This is in agreement with many other studies on 1-hr polar ice (e.g., Llorens, Griera, Bons, Lebensohn, et al., 2016; Llorens, Griera, Bons, Roessiger, et al., 2016; Llorens et al., 2017).

When the temperature is high (300°C) a particular CPO (Figure 9h) that is accompanied by two {100} maxima at 45° between the shear plane and the shear plane normal was observed in torsion experiments (Armann, 2008) at low strain, which our simulations do not reproduce. Armann (2008) refers to it as grain growth CPO and suggests that it is produced by static annealing after deformation ceased in the experiments. Borthwick and Piazolo (2010) carried out thermal annealing experiments (>300°C) on a pre-deformed single crystal halite and found that annealing resulted in a change of the rotation axis of some part of LAGBs and an increase of the LAGBs. Static annealing experiments of olivine aggregates by Boneh et al. (2017) revealed that [100] poles rotate 10°–15° from the original direction during annealing by discontinuous grain growth, in a sample almost composed of porphyroblasts that distinctly have a different CPO from that of the matrix of small grains. The CPO difference between large strain-free grains and surrounding matrix grains was also observed in recrystallized vein quartz (Stöckhert & Duyster, 1999) and chromite (Ghosh et al., 2017). Large free grains are visible in the reflected light micrograph of the experimental microstructure corresponding to the grain growth CPO of Armann (2008) (see Figure 6a of Armann, 2008), which means that discontinuous grain growth took place at high temperature. Therefore, the formation of such CPOs may be influenced by the discontinuous grain growth with anisotropic grain boundary energy (Piazolo et al., 2006) or by the preferred elimination of high-energy grain boundaries during grain growth (Dillon & Rohrer, 2009; Pennock et al., 2009).

4.3. Effect of Temperature on the Misorientation Frequency Distribution of Misorientation: A Strain Gauge?

Figure 10 demonstrates that the frequency distribution of mean subgrain misorientations depends on temperature. At low temperatures (100°C and 200°C) the peak of the misorientation frequency distribution moves positively along the *x*-axis with progressive deformation, accompanied by an increase of the misorientation mean with increasing shear strain. Meanwhile, the skewness of the distribution decreases with increasing shear strain, and the proportion of low-angle subgrain misorientation diminishes, while the frequency of high-angle subgrain misorientation increases (Figures 10a–10j). However, at high temperature (300°C) the mean subgrain misorientation distribution initially raises and then stabilizes with increasing shear strain ($\gamma > 1.0$), while the relative

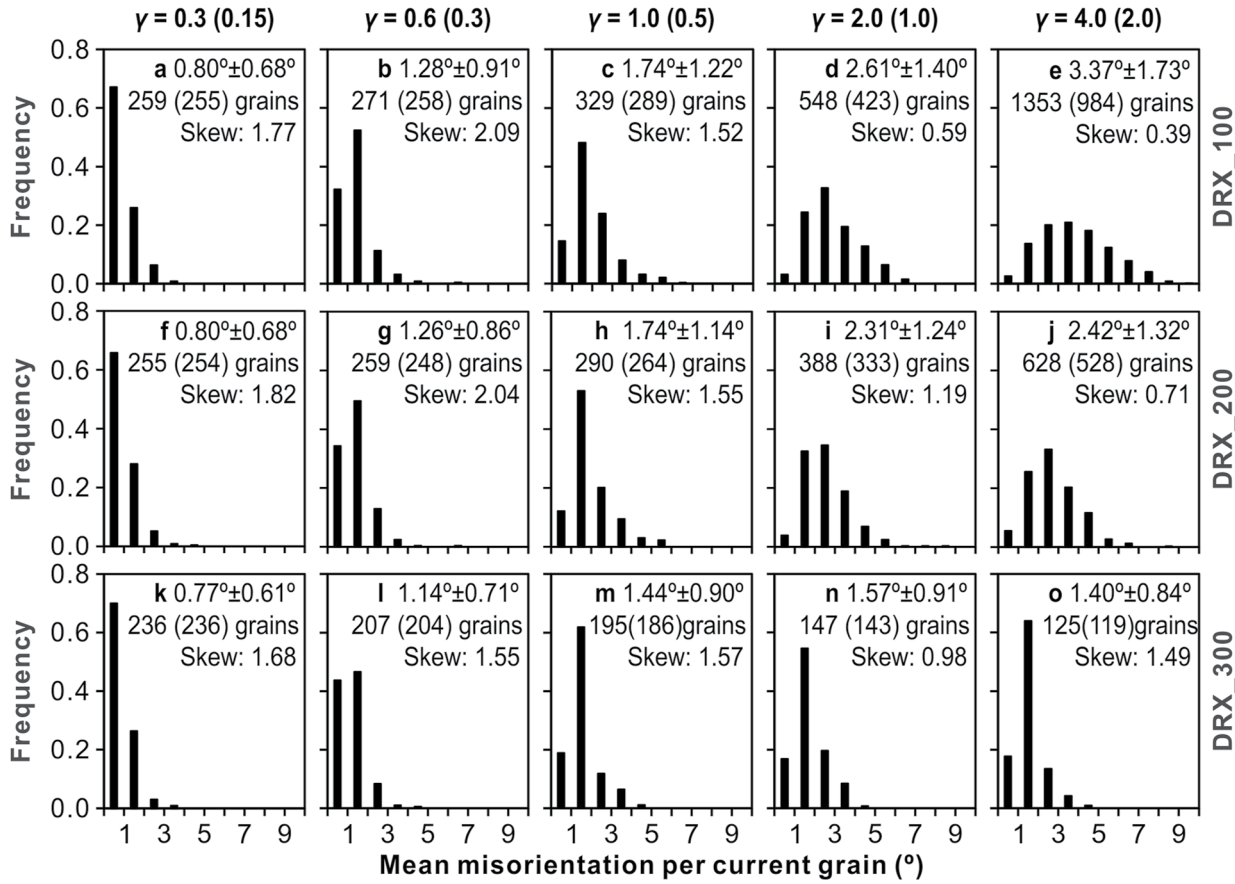

Figure 10. Frequency distribution of grain geometric mean misorientations at the temperature of 100°C, 200°C, and 300°C at different shear strain γ (the value in parentheses is expressed as the natural strain). The geometric means of the misorientation distribution $\theta_{\text{mean-grains}}$ are given along with the standard deviation of the mean. Misorientations were calculated with relevance of the grains that form once the misorientation is above 10°. The value in parentheses corresponds to the number of grains that contain a minimum of 10 crystallites and are considered for use in the strain gauges discussed below. Skewness measures the distribution asymmetry.

abundance of high-angle subgrain misorientation values is low (Figures 10k–10o). Additionally, the frequency distribution of the geometric mean subgrain misorientation subgrains consistently conforms to a positive skew distribution, with the skewness remaining relatively constant at around 1.5 as shear strain increases. Although local boundary and strain stored energies are taken into account for the GBM calculation, the main driving force is the difference in stored strain energy of a grain with respect to its neighbors, during which grains enriched in subgrain boundaries are consumed by grains with no or few LAGBs (Figures 4d–4f). As GBM is enhanced by temperature, this process prevents the formation of 5°–10° subgrain boundaries (Figures 10k–10o), thus explaining the absence of high-angle subgrain boundaries in cases of deformed halite during dynamic recrystallization dominated by GBM (Trimby et al., 2000). At moderate shear strain, there is a remarkable variation of the frequency distributions attending temperatures (Figures 10e, 10j and 10o), with lower values of skewness for lower temperature simulations.

The average subgrain misorientaion across a sample (θ_{av}) displays a power law relationship with natural strain (ε), according to previous studies (Hughes et al., 1998, 2003, 1997; Pantleon, 1997, 1998, 2001; Sethna et al., 2003). These studies suggest that a $\theta_{\text{av}} \sim \varepsilon^n = 2/3$ relationship exists. Pennock and Drury (2005) obtained an exponent of $n = 0.41$ for halite pure shear experiments, while Pennock et al. (2005) estimated an exponent of $n = 0.42$ in similar experiments but measuring misorientations by grain ($\theta_{\text{mean-grains}}$) instead of for the whole sample:

$$\theta_{\text{mean-grains}} = k_1 \varepsilon^n, \tag{7}$$

where k_1 is a constant related to the material and deformation conditions (Hughes et al., 1998, 1997). The setting of the minimum misorientation angle threshold (0.5°, Pennock et al., 2005) in the experimental measurements

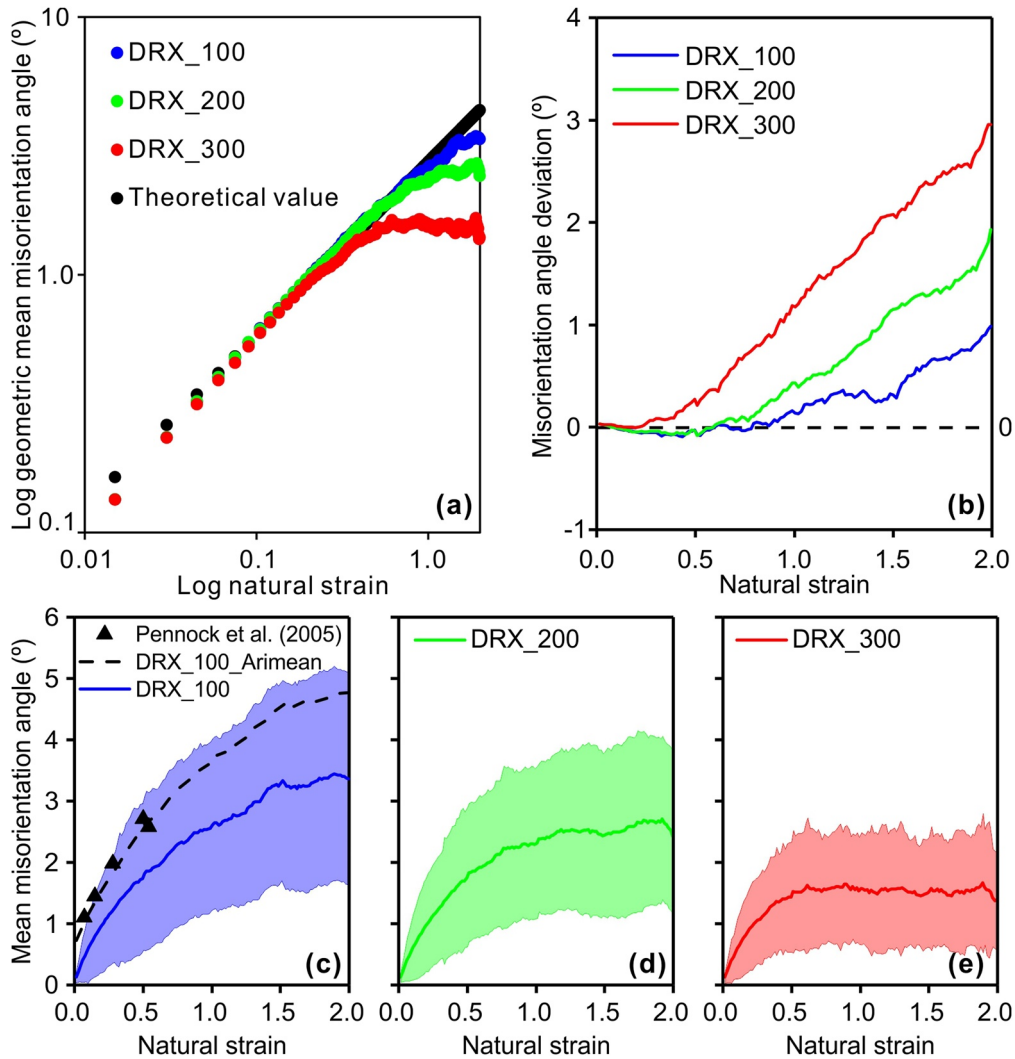

Figure 11. Evolution of the geometric mean of subgrain misorientation with natural strain at temperatures of 100°C (blue), 200°C (green), and 300°C (red), compared with the theoretical power law relationship following Equation 7 ($k_1 = 2.74$, $n = 2/3$; black point). Only grains with at least 10 crystallites are considered in the calculation. (a) Plotted in logarithmic form, log10. (b) Evolution of misorientation deviation from the theoretical power law relationship. (c–e) Evolution of the geometric mean of subgrain misorientation and its standard deviation with natural strain (black dashed line: arithmetic mean of subgrain misorientation, which is higher than 0.5°; black triangle: experimental data from Pennock et al. (2005)).

may lead to an overestimation of the average misorientation angle for low-strain samples due to the limitation of the angular resolution of EBSD (Figure 11), resulting in a lower value of the predicted exponent than the suggested universal exponent of $n = 2/3$. This is confirmed by the strong agreement between the arithmetic mean of misorientation (>0.5°) of DRX_100 simulation and experimental values (Pennock et al., 2005) shown in Figure 11c. In light of the prevalent non-Gaussian misorientation distributions (Figure 10), the employment of the geometric mean as opposed to the arithmetic mean is considered a better fitting metric (Figure 11). Furthermore, it is assumed in our simulations that the recovery process is temperature-independent, that is, the recovery step remains constant for DRX subloops (see Table 2). This assumption is made to allow for a systematic investigation into the impact of GBM on misorientation. We find that, as the level of strain increases, there is a deviation between the geometric mean of misorientation and the corresponding theoretical value (Figures 11a and 11b). As temperature increases, a deviation emerges at lower strain thresholds, specifically from $\varepsilon = 0.81$ at 100°C to $\varepsilon = 0.21$ at 300°C, as illustrated in Figure 11b. Accordingly, the k_1 constant also exhibits dependence on strain and, accordingly, lacks a tangible physical significance. Our simulations show three stages of increasing intracrystalline inhomogeneity, quantified by subgrain boundary misorientation (Figure 11). In the first stage,

the geometric mean of misorientation follows a theoretical power-law relationship with natural strain for models deformed at the whole range of temperatures considered (100–300°C) (Figure 11), as predicted in previous studies of metals (Hughes et al., 1998, 2003, 1997; Pantleon, 1997, 1998, 2001; Sethna et al., 2003). At this stage, lattice distortion and rotation associated with dislocation accumulation dominate, thus causing a misorientation increase following the aforementioned power-law relationship. In the second stage, as strain increases, the increase of geometric mean misorientation slows down significantly and gradually deviates from the theoretical value, with a higher intensity for models deformed at higher temperatures (Figures 11a and 11b). The third stage is characterized by stable misorientation mean values (Figures 11a and 11b), indicating that the generation and annihilation of dislocations within grains are in dynamic equilibrium. As shown in Figure 11b, the misorientation deviation is temperature-dependent, that is, related to the intensity of the dynamic recrystallization in the system. At 100°C GBM plays almost no role (Figure 3), so that the deviation of the mean misorientation at natural strain higher than 0.81 is due to SGR recrystallization. As temperature increases the mean misorientation deviation from the theoretical model takes place at lower strains compared to the 100°C case (Figures 11a and 11b). This is associated with an increase in the GBM intensity that cause a strong reduction of the grain local misorientation by resetting misorientation in zones swept by moving grain boundaries.

In summary, the deviation from the theoretical power law correlates well with the occurrence of two dynamic recrystallization processes: subgrain rotation and GBM. This correlation can be attributed to variations in the rates of DRX processes, which in turn are influenced by changes in temperature. The power-law relationship between the geometric mean of subgrain misorientation and strain exhibits a close conformity with the universal exponent of 2/3, as demonstrated in prior studies. However, it is important to note that this correlation only holds true during the initial deformation stage. In subsequent stages, characterized by pronounced dynamic recrystallization and marked changes in the microstructure, reliance on this relationship may lead to a significant devaluation of natural strain estimations. Hence, the accurate determination of strain gauge necessitates three calibrations of its three stages, or the construction of a theoretical model incorporating factors such as temperature. The study conducted by Stipp et al. (2010) on quartz paleopiezometry demonstrated the requirement for distinct piezometer calibrations for diverse recrystallization processes. For situations in which extensive recrystallization is inferred from natural samples (or experiments), in addition to the geometric mean misorientation as marker to estimate the strain, probably the strain gauge has more potential if it is combined with the skewness of the misorientation distribution (Figure 10 and Figure S2 in Supporting Information S1). In this way, the analysis of the discrepancy between the measured geometric mean misorientation and the skewness of the distribution with respect to the theoretical trend could be used for the prediction of temperature and strain. A reduction of the skewness is expected for low temperature simulations, with limited recrystallization of the polycrystalline aggregate and a higher probability to conserve grains with higher misorientation angles. For the high temperature case, there are observed cycles of accumulation and swept of misorientations produced by larger mobility of grain boundaries, resulting in a higher skewness of the misorientation distribution. However, more systematic analyses would be required to verify these observations.

5. Conclusions

This study presents a novel method to simulate dislocation creep including dynamic recrystallization processes in halite polycrystalline aggregates subjected to simple shear deformation. The VPFFT/ELLE numerical simulation results of simulations run at different temperatures lead to the following conclusions:

1. The proposed full-field approach successfully reproduces the evolution of halite microstructures from laboratory torsion experiments at temperatures of 100–300°C, providing new insights into the competition between grain size reduction by SGR and grain size growth by GBM recrystallization.
2. The intensity of GBM recrystallization, related to temperature, strongly affects the grain morphology and texture, resulting in weaker grain size reduction, more dispersed grain size distributions and more equidimensional grains.
3. Isotropic GBM has little effect on the crystallographic preferred orientation, and it only results in a slightly more intense pole of lattice orientation with respect to cases with no GBM.
4. At low strain the relationship between finite natural strain and the geometric mean subgrain misorientation follows a power law and thus can be used as a strain gauge. However, at high strain the intensity of dynamic recrystallization, including subgrain rotation and GBM, causes a deviation from this the universal scaling law.

The skewness of the frequency distribution of the geometrical mean misorientation can also be used for a better prediction of strain and deformation temperature from the misorientation data.

Data Availability Statement

The software used in this work is open access and can be found in the references cited in the main text and figure captions, as well as in the repository published in Hao et al. (2023a). The data files used in this article are available in Hao et al. (2023b).

Acknowledgments
This study has been funded by DGICYT Spanish Projects PID-2020-118999GB-I00 (Ministerio de Ciencia e Innovación/Agencia Estatal de Investigación/10.13039/501100011033) and PID-2021-122467NB-C21 (Ministerio de Ciencia e Innovación/Agencia Estatal de Investigación/10.13039/501100011033/FEDER), and 2021 SGR 00349 "Geologia Sedimentària" and 2021 SGR 00410 "Modelització Geodinàmica de la Litosfera" (Agència de Gestió d'Ajuts Universitaris i de Recerca). MG-L acknowledges the "Consolidación Investigadora" Grant CNS2022-135819 funded by Ministerio de Ciencia e Innovación/Agencia Estatal de Investigación/10.13039/501100011033 and EU NextGenerationEU/PRTR. Baoqin Hao acknowledges funding by the China Scholarship Council for a PhD scholarship (CSC-202006930010). EG-R acknowledges the "Ramón y Cajal" Fellowship RyC-2018-026335-I, funded by the Ministerio de Ciencia e Innovación/Agencia Estatal de Investigación/10.13039/501100011033. We are grateful to Marina Armann for communication regarding her PhD thesis, and to Till Sachau for helping to create ELLE software containers.

References

Amelirad, O., & Assempour, A. (2022). Coupled continuum damage mechanics and crystal plasticity model and its application in damage evolution in polycrystalline aggregates. *Engineering with Computers*, *38*(S3), 2121–2135. https://doi.org/10.1007/s00366-021-01346-2

Armann, M. (2008). *Microstructural and textural development in synthetic rocksalt deformed in torsion* (Doctoral dissertation). ETH-Zurich. https://doi.org/10.3929/ethz-a-005666840

Bachmann, F., Hielscher, R., & Schaeben, H. (2010). Texture analysis with MTEX – Free and open source software toolbox. *Solid State Phenomena*, *160*, 63–68. https://doi.org/10.4028/www.scientific.net/SSP.160.63

Becker, J. K., Bons, P. D., & Jessell, M. W. (2008). A new front-tracking method to model anisotropic grain and phase boundary motion in rocks. *Computers & Geosciences*, *34*(3), 201–212. https://doi.org/10.1016/j.cageo.2007.03.013

Bestmann, M., Piazolo, S., Spiers, C. J., & Prior, D. J. (2005). Microstructural evolution during initial stages of static recovery and recrystallization: New insights from in-situ heating experiments combined with electron backscatter diffraction analysis. *Journal of Structural Geology*, *27*(3), 447–457. https://doi.org/10.1016/j.jsg.2004.10.006

Boneh, Y., Wallis, D., Hansen, L. N., Krawczynski, M. J., & Skemer, P. (2017). Oriented grain growth and modification of 'frozen anisotropy' in the lithospheric mantle. *Earth and Planetary Science Letters*, *474*, 368–374. https://doi.org/10.1016/j.epsl.2017.06.050

Bons, P. D., Koehn, D., & Jessell, M. W. (Eds.). (2008). *Microdynamics simulation* (Vol. 106). Springer. https://doi.org/10.1007/978-3-540-44793-1

Bons, P. D., & Urai, J. L. (1992). Syndeformational grain growth: Microstructures and kinetics. *Journal of Structural Geology*, *14*(8–9), 1101–1109. https://doi.org/10.1016/0191-8141(92)90038-X

Borthwick, V. E., & Piazolo, S. (2010). Post-deformational annealing at the subgrain scale: Temperature dependent behaviour revealed by in-situ heating experiments on deformed single crystal halite. *Journal of Structural Geology*, *32*(7), 982–996. https://doi.org/10.1016/j.jsg.2010.06.006

Borthwick, V. E., Piazolo, S., Evans, L., Griera, A., & Bons, P. D. (2014). What happens to deformed rocks after deformation? A refined model for recovery based on numerical simulations. *Geological Society, London, Special Publications*, *394*(1), 215–234. https://doi.org/10.1144/SP394.11

Bourcier, M., Bornert, M., Dimanov, A., Héripré, E., & Raphanel, J. L. (2013). Multiscale experimental investigation of crystal plasticity and grain boundary sliding in synthetic halite using digital image correlation. *Journal of Geophysical Research: Solid Earth*, *118*(2), 511–526. https://doi.org/10.1002/jgrb.50065

Bruno, M., Aquilano, D., Pastero, L., & Prencipe, M. (2008). Structures and surface energies of (100) and octopolar (111) faces of halite (NaCl): An ab initio quantum-mechanical and thermodynamical study. *Crystal Growth & Design*, *8*(7), 2163–2170. https://doi.org/10.1021/cg8000027

Canérot, J., Hudec, M. R., & Rockenbauch, K. (2005). Mesozoic diapirism in the Pyrenean orogen: Salt tectonics on a transform plate boundary. *AAPG Bulletin*, *89*(2), 211–229. https://doi.org/10.1306/09170404007

Carter, N. L., & Heard, H. C. (1970). Temperature and rate dependent deformation of halite. *American Journal of Science*, *269*(3), 193–249. https://doi.org/10.2475/ajs.269.3.193

Carter, N. L., Horseman, S. T., Russell, J. E., & Handin, J. (1993). Rheology of rocksalt. *Journal of Structural Geology*, *15*(9–10), 1257–1271. https://doi.org/10.1016/0191-8141(93)90168-A

de Riese, T., Evans, L., Gomez-Rivas, E., Griera, A., Lebensohn, R. A., Llorens, M.-G., et al. (2019). Shear localisation in anisotropic, non-linear viscous materials that develop a CPO: A numerical study. *Journal of Structural Geology*, *124*, 81–90. https://doi.org/10.1016/j.jsg.2019.03.006

Desbois, G., Závada, P., Schléder, Z., & Urai, J. L. (2010). Deformation and recrystallization mechanisms in actively extruding salt fountain: Microstructural evidence for a switch in deformation mechanisms with increased availability of meteoric water and decreased grain size (Qum Kuh, central Iran). *Journal of Structural Geology*, *32*(4), 580–594. https://doi.org/10.1016/j.jsg.2010.03.005

Dillon, S. J., & Rohrer, G. S. (2009). Mechanism for the development of anisotropic grain boundary character distributions during normal grain growth. *Acta Materialia*, *57*(1), 1–7. https://doi.org/10.1016/j.actamat.2008.08.062

Drury, M. R., & Urai, J. L. (1990). Deformation-related recrystallization processes. *Tectonophysics*, *172*(3–4), 235–253. https://doi.org/10.1016/0040-1951(90)90033-5

Eisenlohr, P., Diehl, M., Lebensohn, R. A., & Roters, F. (2013). A spectral method solution to crystal elasto-viscoplasticity at finite strains. *International Journal of Plasticity*, *46*, 37–53. https://doi.org/10.1016/j.ijplas.2012.09.012

Finch, M. A., Bons, P. D., Steinbach, F., Griera, A., Llorens, M.-G., Gomez-Rivas, E., et al. (2020). The ephemeral development of C′ shear bands: A numerical modelling approach. *Journal of Structural Geology*, *139*, 104091. https://doi.org/10.1016/j.jsg.2020.104091

Finch, M. A., Bons, P. D., Weinberg, R. F., Llorens, M.-G., Griera, A., & Gomez-Rivas, E. (2022). A dynamic atlas of interference patterns in superimposed, opposite sense ductile shear zones. *Journal of Structural Geology*, *165*, 104739. https://doi.org/10.1016/j.jsg.2022.104739

Fossen, H. (2010). Deformation bands formed during soft-sediment deformation: Observations from SE Utah. *Marine and Petroleum Geology*, *27*(1), 215–222. https://doi.org/10.1016/j.marpetgeo.2009.06.005

Franssen, R. C. M. W. (1994). The rheology of synthetic rocksalt in uniaxial compression. *Tectonophysics*, *233*(1–2), 1–40. https://doi.org/10.1016/0040-1951(94)90218-6

Franssen, R. C. M. W., & Spiers, C. J. (1990). Deformation of polycrystalline salt in compression and in shear at 250–350°C. *Geological Society, London, Special Publications*, *54*(1), 201–213. https://doi.org/10.1144/GSL.SP.1990.054.01.20

Frost, H. J., & Ashby, M. F. (1982). *Deformation-mechanism maps: The plasticity and creep of metals and ceramics* (175 pp.). Pergamon Press.

Ghosh, B., Misra, S., & Morishita, T. (2017). Plastic deformation and post-deformation annealing in chromite: Mechanisms and implications. *American Mineralogist*, *102*(1), 216–226. https://doi.org/10.2138/am-2017-5709

Gomez-Rivas, E., Butler, R. W. H., Healy, D., & Alsop, I. (2020). From hot to cold – The temperature dependence on rock deformation processes: An introduction. *Journal of Structural Geology*, *132*, 103977. https://doi.org/10.1016/j.jsg.2020.103977

Gomez-Rivas, E., Griera, A., Llorens, M.-G., Bons, P. D., Lebensohn, R. A., & Piazolo, S. (2017). Subgrain rotation recrystallization during shearing: Insights from full-field numerical simulations of halite polycrystals. *Journal of Geophysical Research: Solid Earth*, *122*(11), 8810–8827. https://doi.org/10.1002/2017JB014508

Griera, A., Bons, P. D., Jessell, M. W., Lebensohn, R. A., Evans, L., & Gomez-Rivas, E. (2011). Strain localization and porphyroclast rotation. *Geology*, *39*(3), 275–278. https://doi.org/10.1130/G31549.1

Griera, A., Llorens, M.-G., Gomez-Rivas, E., Bons, P. D., Jessell, M. W., Evans, L. A., & Lebensohn, R. (2013). Numerical modelling of porphyroclast and porphyroblast rotation in anisotropic rocks. *Tectonophysics*, *587*, 4–29. https://doi.org/10.1016/j.tecto.2012.10.008

Guillope, M., & Poirier, J. P. (1979). Dynamic recrystallization during creep of single-crystalline halite: An experimental study. *Journal of Geophysical Research*, *84*(B10), 5557–5567. https://doi.org/10.1029/JB084iB10p05557

Hao, B., Llorens, M.-G., Griera Artigas, A., Bons, P. D., Lebensohn, R., Yu, Y., & Gomez-Rivas, E. (2023a). Full-field numerical simulation of halite dynamic recrystallization from subgrain rotation to grain boundary migration [Software]. Journal of Geophysical Research Solid Earth (1.0). Zenodo. https://doi.org/10.5281/zenodo.10259841

Hao, B., Llorens, M.-G., Griera, A., Bons, P. D., Lebensohn, R. A., Yu, Y., & Gómez-Rivas, E. (2023b). Full-field numerical simulations of sub grain rotation and grain boundary migration in halite during viscoplastic deformation [Dataset]. DIGITAL.CSIC. https://doi.org/10.20350/digitalCSIC/15474

Henneberg, M., Linckens, J., Schramm, M., Hammer, J., Gerdes, A., & Zulauf, G. (2020). Structural evolution of continental and marine Permian rock salt of the North German basin: Constraints from microfabrics, geochemistry and U–Pb ages. *International Journal of Earth Sciences*, *109*(7), 2369–2387. https://doi.org/10.1007/s00531-020-01905-w

Hirth, G., & Tullis, J. (1992). Dislocation creep regimes in quartz aggregates. *Journal of Structural Geology*, *14*(2), 145–159. https://doi.org/10.1016/0191-8141(92)90053-Y

Hudec, M. R., & Jackson, M. P. A. (2007). Terra infirma: Understanding salt tectonics. *Earth-Science Reviews*, *82*(1–2), 1–28. https://doi.org/10.1016/j.earscirev.2007.01.001

Hughes, D. A., Chrzan, D. C., Liu, Q., & Hansen, N. (1998). Scaling of misorientation angle distributions. *Physical Review Letters*, *81*(21), 4664–4667. https://doi.org/10.1103/PhysRevLett.81.4664

Hughes, D. A., & Hansen, N. (2018). The microstructural origin of work hardening stages. *Acta Materialia*, *148*, 374–383. https://doi.org/10.1016/j.actamat.2018.02.002

Hughes, D. A., Hansen, N., & Bammann, D. J. (2003). Geometrically necessary boundaries, incidental dislocation boundaries and geometrically necessary dislocations. *Scripta Materialia*, *48*(2), 147–153. https://doi.org/10.1016/S1359-6462(02)00358-5

Hughes, D. A., Liu, Q., Chrzan, D. C., & Hansen, N. (1997). Scaling of microstructural parameters: Misorientations of deformation induced boundaries. *Acta Materialia*, *45*(1), 105–112. https://doi.org/10.1016/S1359-6454(96)00153-X

Hunsche, U., & Hampel, A. (1999). Rock salt — The mechanical properties of the host rock material for a radioactive waste repository. *Engineering Geology*, *52*(3–4), 271–291. https://doi.org/10.1016/S0013-7952(99)00011-3

Jessell, M. W., Bons, P. D., Evans, L., Barr, T., & Stüwe, K. (2001). Elle: The numerical simulation of metamorphic and deformation microstructures. *Computers & Geosciences*, *27*(1), 17–30. https://doi.org/10.1016/S0098-3004(00)00061-3

Jessell, M. W., Bons, P. D., Griera, A., Evans, L. A., & Wilson, C. J. L. (2009). A tale of two viscosities. *Journal of Structural Geology*, *31*(7), 719–736. https://doi.org/10.1016/j.jsg.2009.04.010

Jessell, M. W., Kostenko, O., & Jamtveit, B. (2003). The preservation potential of microstructures during static grain growth. *Journal of Metamorphic Geology*, *21*(5), 481–491. https://doi.org/10.1046/j.1525-1314.2003.00455.x

Kaminski, É., & Ribe, N. M. (2001). A kinematic model for recrystallization and texture development in olivine polycrystals. *Earth and Planetary Science Letters*, *189*(3–4), 253–267. https://doi.org/10.1016/S0012-821X(01)00356-9

Kaminski, É., Ribe, N. M., & Browaeys, J. T. (2004). D-Rex, a program for calculation of seismic anisotropy due to crystal lattice preferred orientation in the convective upper mantle. *Geophysical Journal International*, *158*(2), 744–752. https://doi.org/10.1111/j.1365-246X.2004.02308.x

Karato, S. (2008). *Deformation of earth materials. An introduction to the rheology of Solid Earth* (Vol. 463). Cambridge Press.

Lebensohn, R. A. (2001). N-site modeling of a 3D viscoplastic polycrystal using Fast Fourier Transform. *Acta Materialia*, *49*(14), 2723–2737. https://doi.org/10.1016/S1359-6454(01)00172-0

Lebensohn, R. A., Dawson, P. R., Kern, H. M., & Wenk, H.-R. (2003). Heterogeneous deformation and texture development in halite polycrystals: Comparison of different modeling approaches and experimental data. *Tectonophysics*, *370*(1–4), 287–311. https://doi.org/10.1016/S0040-1951(03)00192-6

Lebensohn, R. A., & Rollett, A. D. (2020). Spectral methods for full-field micromechanical modelling of polycrystalline materials. *Computational Materials Science*, *173*, 109336. https://doi.org/10.1016/j.commatsci.2019.109336

Lebensohn, R. A., & Tomé, C. N. (1993). A self-consistent anisotropic approach for the simulation of plastic deformation and texture development of polycrystals: Application to zirconium alloys. *Acta Metallurgica et Materialia*, *41*(9), 2611–2624. https://doi.org/10.1016/0956-7151(93)90130-K

Leitner, C., Neubauer, F., Urai, J. L., & Schoenherr, J. (2011). Structure and evolution of a rocksalt-mudrock-tectonite: The haselgebirge in the Northern Calcareous Alps. *Journal of Structural Geology*, *33*(5), 970–984. https://doi.org/10.1016/j.jsg.2011.02.008

Linckens, J., Zulauf, G., & Hammer, J. (2016). Experimental deformation of coarse-grained rock salt to high strain. *Journal of Geophysical Research: Solid Earth*, *121*(8), 6150–6171. https://doi.org/10.1002/2016JB012890

Liu, Y., Gilormini, P., & Castañeda, P. P. (2005). Homogenization estimates for texture evolution in halite. *Tectonophysics*, *406*(3–4), 179–195. https://doi.org/10.1016/j.tecto.2005.06.007

Llorens, M.-G., Gomez-Rivas, E., Ganzhorn, A.-C., Griera, A., Steinbach, F., Roessiger, J., et al. (2019). The effect of dynamic recrystallisation on the rheology and microstructures of partially molten rocks. *Journal of Structural Geology*, *118*, 224–235. https://doi.org/10.1016/j.jsg.2018.10.013

Llorens, M.-G., Griera, A., Bons, P. D., Lebensohn, R. A., Evans, L. A., Jansen, D., & Weikusat, I. (2016). Full-field predictions of ice dynamic recrystallisation under simple shear conditions. *Earth and Planetary Science Letters*, *450*, 233–242. https://doi.org/10.1016/j.epsl.2016.06.045

Llorens, M.-G., Griera, A., Bons, P. D., Roessiger, J., Lebensohn, R., Evans, L., & Weikusat, I. (2016). Dynamic recrystallisation of ice aggregates during co-axial viscoplastic deformation: A numerical approach. *Journal of Glaciology*, *62*(232), 359–377. https://doi.org/10.1017/jog.2016.28

Llorens, M.-G., Griera, A., Steinbach, F., Bons, P. D., Gomez-Rivas, E., Jansen, D., et al. (2017). Dynamic recrystallization during deformation of polycrystalline ice: Insights from numerical simulations. *Philosophical Transactions of the Royal Society A: Mathematical, Physical & Engineering Sciences*, *375*(2086), 20150346. https://doi.org/10.1098/rsta.2015.0346

Lücke, K., & Stüwe, H. P. (1971). On the theory of impurity controlled grain boundary motion. *Acta Metallurgica*, *19*(10), 1087–1099. https://doi.org/10.1016/0001-6160(71)90041-1

Mainprice, D., Hielscher, R., & Schaeben, H. (2011). Calculating anisotropic physical properties from texture data using the MTEX open-source package. *Geological Society, London, Special Publications*, *360*(1), 175–192. https://doi.org/10.1144/SP360.10

Mansouri, H., Prior, D. J., Ajalloeian, R., & Elyaszadeh, R. (2019). Deformation and recrystallization mechanisms inferred from microstructures of naturally deformed rock salt from the diapiric stem and surface glaciers of a salt diapir in Southern Iran. *Journal of Structural Geology*, *121*, 10–24. https://doi.org/10.1016/j.jsg.2019.01.005

Marques, F. O., Burg, J.-P., Armann, M., & Martinho, E. (2013). Rheology of synthetic polycrystalline halite in torsion. *Tectonophysics*, *583*, 124–130. https://doi.org/10.1016/j.tecto.2012.10.024

McClay, K., Muñoz, J.-A., & García-Senz, J. (2004). Extensional salt tectonics in a contractional orogen: A newly identified tectonic event in the Spanish Pyrenees. *Geology*, *32*(9), 737. https://doi.org/10.1130/G20565.1

Mika, D. P., & Dawson, P. R. (1999). Polycrystal plasticity modeling of intracrystalline boundary textures. *Acta Materialia*, *47*(4), 1355–1369. https://doi.org/10.1016/S1359-6454(98)00386-3

Moulinec, H., & Suquet, P. (1994). A fast numerical method for computing the linear and nonlinear mechanical properties of composites. *Comptes Rendus de l'Académie Des Sciences. Série II. Mécanique, Physique, Chimie, Astronomie*, 1417–1423. Retrieved from https://hal.science/hal-03019226/document

Moulinec, H., & Suquet, P. (1998). A numerical method for computing the overall response of nonlinear composites with complex microstructure. *Computer Methods in Applied Mechanics and Engineering*, *157*(1–2), 69–94. https://doi.org/10.1016/S0045-7825(97)00218-1

Olgaard, D. L., & Evans, B. (1988). Grain growth in synthetic marbles with added mica and water. *Contributions to Mineralogy and Petrology*, *100*(2), 246–260. https://doi.org/10.1007/BF00373591

Otsuka, T., Brenner, R., & Bacroix, B. (2018). FFT-based modelling of transformation plasticity in polycrystalline materials during diffusive phase transformation. *International Journal of Engineering Science*, *127*, 92–113. https://doi.org/10.1016/j.ijengsci.2018.02.008

Pantleon, W. (1997). On the evolution of disorientations in dislocation cell structures during plastic deformation. *Materials Science and Engineering: A*, *234–236*, 567–570. https://doi.org/10.1016/S0921-5093(97)00227-X

Pantleon, W. (1998). On the statistical origin of disorientations in dislocation structures. *Acta Materialia*, *46*(2), 451–456. https://doi.org/10.1016/S1359-6454(97)00286-3

Pantleon, W. (2001). The evolution of disorientations for several types of boundaries. *Materials Science and Engineering: A*, *319–321*, 211–215. https://doi.org/10.1016/S0921-5093(01)00947-9

Paterson, M. S., & Olgaard, D. L. (2000). Rock deformation tests to large shear strains in torsion. *Journal of Structural Geology*, *22*(9), 1341–1358. https://doi.org/10.1016/S0191-8141(00)00042-0

Peach, C. J., & Spiers, C. J. (1996). Influence of crystal plastic deformation on dilatancy and permeability development in synthetic salt rock. *Tectonophysics*, *256*(1–4), 101–128. https://doi.org/10.1016/0040-1951(95)00170-0

Peach, C. J., Spiers, C. J., & Trimby, P. W. (2001). Effect of confining pressure on dilatation, recrystallization, and flow of rock salt at 150°C. *Journal of Geophysical Research*, *106*(B7), 13315–13328. https://doi.org/10.1029/2000JB900300

Pennock, G. M., Coleman, M., Drury, M. R., & Randle, V. (2009). Grain boundary plane populations in minerals: The example of wet NaCl after low strain deformation. *Contributions to Mineralogy and Petrology*, *158*(1), 53–67. https://doi.org/10.1007/s00410-008-0370-5

Pennock, G. M., & Drury, M. R. (2005). Low-angle subgrain misorientations in deformed NaCl. *Journal of Microscopy*, *217*(2), 130–137. https://doi.org/10.1111/j.1365-2818.2005.01410.x

Pennock, G. M., Drury, M. R., & Spiers, C. J. (2005). The development of subgrain misorientations with strain in dry synthetic NaCl measured using EBSD. *Journal of Structural Geology*, *27*(12), 2159–2170. https://doi.org/10.1016/j.jsg.2005.06.013

Pennock, G. M., Drury, M. R., Trimby, P. W., & Spiers, C. J. (2002). Misorientation distributions in hot deformed NaCl using electron backscattered diffraction. *Journal of Microscopy*, *208*(1), 75. https://doi.org/10.1046/j.1365-2818.2002.00993.x

Piazolo, S., Bestmann, M., Prior, D. J., & Spiers, C. J. (2006). Temperature dependent grain boundary migration in deformed-then-annealed material: Observations from experimentally deformed synthetic rocksalt. *Tectonophysics*, *427*(1–4), 55–71. https://doi.org/10.1016/j.tecto.2006.06.007

Piazolo, S., Bons, P. D., Griera, A., Llorens, M.-G., Gomez-Rivas, E., Koehn, D., et al. (2019). A review of numerical modelling of the dynamics of microstructural development in rocks and ice: Past, present and future. *Journal of Structural Geology*, *125*, 111–123. https://doi.org/10.1016/j.jsg.2018.05.025

Picard, D., Dimanov, A., & Raphanel, J. L. (2018). Plastic behavior of halite single-crystals at different temperatures and strain rates: New insights from in-situ experiments and full field measures. *Materials Science and Engineering: A*, *732*, 284–297. https://doi.org/10.1016/j.msea.2018.07.009

Pokharel, R., Lind, J., Kanjarla, A. K., Lebensohn, R. A., Li, S. F., Kenesei, P., et al. (2014). Polycrystal plasticity: Comparison between grain-scale observations of deformation and simulations. *Annual Review of Condensed Matter Physics*, *5*(1), 317–346. https://doi.org/10.1146/annurev-conmatphys-031113-133846

Radhakrishnan, B., & Sarma, G. B. (2008). Coupled simulations of texture evolution during deformation and recrystallization of fcc and bcc metals. *Materials Science and Engineering: A*, *494*(1–2), 73–79. https://doi.org/10.1016/j.msea.2007.10.094

Ran, H., Bons, P. D., Wang, G., Griera, A., de Riese, T., Gomez-Rivas, E., et al. (2022). Folds inside pebbles: When do they form during conglomerate deformation? Numerical modelling and comparison with the Hutuo group conglomerates, North China Craton. *Journal of Structural Geology*, *160*, 104620. https://doi.org/10.1016/j.jsg.2022.104620

Ran, H., Bons, P. D., Wang, G., Steinbach, F., Finch, M. A., Griera, A., et al. (2018). High-strain deformation of conglomerates: Numerical modelling, strain analysis, and an example from the Wutai Mountains, North China Craton. *Journal of Structural Geology*, *114*, 222–234. https://doi.org/10.1016/j.jsg.2018.06.018

Ran, H., de Riese, T., Llorens, M.-G., Finch, M. A., Evans, L. A., Gomez-Rivas, E., et al. (2019). Time for anisotropy: The significance of mechanical anisotropy for the development of deformation structures. *Journal of Structural Geology*, *125*, 41–47. https://doi.org/10.1016/j.jsg.2018.04.019

Randle, V. (1993). Microtexture investigation of the relationship between strain and anomalous grain growth. *Philosophical Magazine A*, *67*(6), 1301–1313. https://doi.org/10.1080/01418619308225356

Read, W. T., & Shockley, W. (1950). Dislocation models of crystal grain boundaries. *Physical Review*, *78*(3), 275–289. https://doi.org/10.1103/PhysRev.78.275

Roessiger, J., Bons, P. D., Griera, A., Jessell, M. W., Evans, L., Montagnat, M., et al. (2011). Competition between grain growth and grain-size reduction in polar ice. *Journal of Glaciology*, *57*(205), 942–948. https://doi.org/10.3189/002214311798043690

Rohrer, G. S. (2011). Grain boundary energy anisotropy: A review. *Journal of Materials Science*, *46*(18), 5881–5895. https://doi.org/10.1007/s10853-011-5677-3

Roters, F., Eisenlohr, P., Hantcherli, L., Tjahjanto, D. D., Bieler, T. R., & Raabe, D. (2010). Overview of constitutive laws, kinematics, homogenization and multiscale methods in crystal plasticity finite-element modeling: Theory, experiments, applications. *Acta Materialia*, *58*(4), 1152–1211. https://doi.org/10.1016/j.actamat.2009.10.058

Schléder, Z., & Urai, J. L. (2005). Microstructural evolution of deformation-modified primary halite from the Middle Triassic Röt formation at Hengelo, The Netherlands. *International Journal of Earth Sciences*, *94*(5–6), 941–955. https://doi.org/10.1007/s00531-005-0503-2

Schléder, Z., & Urai, J. L. (2007). Deformation and recrystallization mechanisms in mylonitic shear zones in naturally deformed extrusive Eocene–Oligocene rocksalt from Eyvanekey plateau and Garmsar hills (central Iran). *Journal of Structural Geology*, *29*(2), 241–255. https://doi.org/10.1016/j.jsg.2006.08.014

Sethna, J. P., Coffman, V. R., & Demler, E. (2003). Scaling in plasticity-induced cell-boundary microstructure: Fragmentation and rotational diffusion. *Physical Review B*, *67*(18), 184107. https://doi.org/10.1103/PhysRevB.67.184107

Signorelli, J., & Tommasi, A. (2015). Modeling the effect of subgrain rotation recrystallization on the evolution of olivine crystal preferred orientations in simple shear. *Earth and Planetary Science Letters*, *430*, 356–366. https://doi.org/10.1016/j.epsl.2015.08.018

Spiers, C. J., Peach, C. J., Brzesowsky, R. H., Schutjens, P. M. T. M., Liezenberg, J. L., & Zwart, H. J. (1988). *Long-term rheological and transport properties of dry and wet salt rocks*. Office for Official Publications of the European Communities.

Spiers, C. J., Schutjens, P. M. T. M., Brzesowsky, R. H., Peach, C. J., Liezenberg, J. L., & Zwart, H. J. (1990). Experimental determination of constitutive parameters governing creep of rocksalt by pressure solution. *Geological Society, London, Special Publications*, *54*(1), 215–227. https://doi.org/10.1144/GSL.SP.1990.054.01.21

Steinbach, F., Bons, P. D., Griera, A., Jansen, D., Llorens, M.-G., Roessiger, J., & Weikusat, I. (2016). Strain localization and dynamic recrystallization in the ice–air aggregate: A numerical study. *The Cryosphere*, *10*(6), 3071–3089. https://doi.org/10.5194/tc-10-3071-2016

Steinbach, F., Kuiper, E.-J. N., Eichler, J., Bons, P. D., Drury, M. R., Griera, A., et al. (2017). The relevance of grain dissection for grain size reduction in polar ice: Insights from numerical models and ice core microstructure analysis. *Frontiers in Earth Science*, *5*. https://doi.org/10.3389/feart.2017.00066

Stipp, M., Stünitz, H., Heilbronner, R., & Schmid, S. M. (2002). The eastern Tonale fault zone: A 'natural laboratory' for crystal plastic deformation of quartz over a temperature range from 250 to 700°C. *Journal of Structural Geology*, *24*(12), 1861–1884. https://doi.org/10.1016/S0191-8141(02)00035-4

Stipp, M., Tullis, J., Scherwath, M., & Behrmann, J. H. (2010). A new perspective on paleopiezometry: Dynamically recrystallized grain size distributions indicate mechanism changes. *Geology*, *38*(8), 759–762. https://doi.org/10.1130/G31162.1

Stöckhert, B., & Duyster, J. (1999). Discontinuous grain growth in recrystallised vein quartz — Implications for grain boundary structure, grain boundary mobility, crystallographic preferred orientation, and stress history. *Journal of Structural Geology*, *21*(10), 1477–1490. https://doi.org/10.1016/S0191-8141(99)00084-X

Sun, R. C., & Bauer, C. L. (1970). Tilt boundary migration in NaCl bicrystals. *Acta Metallurgica*, *18*(6), 639–647. https://doi.org/10.1016/0001-6160(70)90093-3

ter Heege, J. H., de Bresser, J. H. P., & Spiers, C. J. (2004). Dynamic recrystallization of dense polycrystalline NaCl: Dependence of grain size distribution on stress and temperature. *Materials Science Forum*, *467–470*, 1187–1192. https://doi.org/10.4028/www.scientific.net/MSF.467-470.1187

ter Heege, J. H., de Bresser, J. H. P., & Spiers, C. J. (2005a). Dynamic recrystallization of wet synthetic polycrystalline halite: Dependence of grain size distribution on flow stress, temperature and strain. *Tectonophysics*, *396*(1–2), 35–57. https://doi.org/10.1016/j.tecto.2004.10.002

ter Heege, J. H., de Bresser, J. H. P., & Spiers, C. J. (2005b). Rheological behaviour of synthetic rocksalt: The interplay between water, dynamic recrystallization and deformation mechanisms. Journal of Structural Geology, *27*, 948–963. https://doi.org/10.1016/j.jsg.2005.04.008

Thiemeyer, N., Zulauf, G., Mertineit, M., Linckens, J., Pusch, M., & Hammer, J. (2016). Microfabrics and 3D grain shape of Gorleben rock salt: Constraints on deformation mechanisms and paleodifferential stress. *Tectonophysics*, *676*, 1–19. https://doi.org/10.1016/j.tecto.2016.02.046

Trimby, P. W., Drury, M. R., & Spiers, C. J. (2000). Recognising the crystallographic signature of recrystallisation processes in deformed rocks: A study of experimentally deformed rocksalt. *Journal of Structural Geology*, *22*(11–12), 1609–1620. https://doi.org/10.1016/S0191-8141(00)00059-6

Urai, J. L., Means, W. D., & Lister, G. S. (1986). Dynamic recrystallization of minerals. In B. E. Hobbs & H. C. Heard (Eds.), *Mineral and rock deformation: Laboratory studies: The Paterson Volume* (Vol. 36, pp. 161–199). American Geophysical Union. https://doi.org/10.1029/GM036p0161

Urai, J. L., Schléder, Z., Spiers, C. J., & Kukla, P. A. (2008). Flow and transport properties of salt rocks. In R. Littke, U. Bayer, D. Gajewski, & S. Nelskamp (Eds.), *Dynamics of complex intracontinental basins: The central European basin system* (pp. 277–290). Springer.

Wawersik, W. R., & Zeuch, D. H. (1986). Modeling and mechanistic interpretation of creep of rock salt below 200°C. *Tectonophysics*, *121*(2–4), 125–152. https://doi.org/10.1016/0040-1951(86)90040-5

Weaire, D., & Rivier, N. (1984). Soap, cells and statistics—Random patterns in two dimensions. *Contemporary Physics*, *25*(1), 59–99. https://doi.org/10.1080/00107518408210979

Wenk, H.-R., Armann, M., Burlini, L., Kunze, K., & Bortolotti, M. (2009). Large strain shearing of halite: Experimental and theoretical evidence for dynamic texture changes. *Earth and Planetary Science Letters*, *280*(1–4), 205–210. https://doi.org/10.1016/j.epsl.2009.01.036

Wenk, H.-R., Bennett, K., Canova, G. R., & Molinari, A. (1991). Modelling plastic deformation of peridotite with the self-consistent theory. *Journal of Geophysical Research*, *96*(B5), 8337–8349. https://doi.org/10.1029/91JB00117